J. Math. Fluid Mech. (2021) 23:64

https://doi.org/10.1007/s00021-021-00593-z

Journal of Mathematical Fluid Mechanics

# Refactorization of Cauchy's Method: A Second-Order Partitioned Method for Fluid–Thick Structure Interaction Problems

Martina Bukač, Anyastassia Seboldt and Catalin Trenchea

*Communicated by F. Gazzola*

**Abstract.** This work focuses on the derivation and the analysis of a novel, strongly-coupled partitioned method for fluid–structure interaction problems. The flow is assumed to be viscous and incompressible, and the structure is modeled using linear elastodynamics equations. We assume that the structure is thick, i.e., modeled using the same number of spatial dimensions as fluid. Our newly developed numerical method is based on Robin boundary conditions, as well as on the refactorization of the Cauchy's one-legged '$\theta$-like' method, written as a sequence of Backward Euler–Forward Euler steps used to discretize the problem in time. This family of methods, parametrized by $\theta$, is B-stable for any $\theta \in [\frac{1}{2}, 1]$ and second-order accurate for $\theta = \frac{1}{2} + \mathcal{O}(\tau)$, where $\tau$ is the time step. In the proposed algorithm, the fluid and structure sub-problems, discretized using the Backward Euler scheme, are first solved iteratively until convergence. Then, the variables are linearly extrapolated, equivalent to solving Forward Euler problems. We prove that the iterative procedure is convergent, and that the proposed method is stable provided $\theta \in [\frac{1}{2}, 1]$. Numerical examples, based on the finite element discretization in space, explore convergence rates using different values of parameters in the problem, and compare our method to other strongly-coupled partitioned schemes from the literature. We also compare our method to both a monolithic and a non-iterative partitioned solver on a benchmark problem with parameters within the physiological range of blood flow, obtaining an excellent agreement with the monolithic scheme.

**Mathematics Subject Classification.** Primary 65M12, Secondary 76Z05.

**Keywords.** Fluid–structure interaction, Partitioned scheme, Second-order convergence, Strongly-coupled.

## 1. Introduction

Fluid–structure interaction (FSI) describes a specific type of problem that involves the highly non-linear relationship between a fluid and deformable structure. The importance of solving FSI problems is made clear when one simply sits back to observe everyday life – in the wind that blows across an airplane wing or bridge, a vessel or fish that ventures across the ocean, or even someone's heart sending a pulse of blood through an artery. Since these ubiquitous occurrences cannot be over-emphasized with their pertinent applications in the biomedical, engineering, and architectural realms, FSI problems have received a lot of attention from both theoretical and computational perspectives. In particular, with increasing medical demand revolving around hemodynamics-related problems, engineering advancements for the understanding and improvement of aeronautical and naval applications, and demand for more sustainable energy harvesting, there is a high demand for fast and accurate numerical solvers for FSI problems.

Two main methodologies for numerically solving FSI problems are monolithic and partitioned schemes. Both monolithic and partitioned algorithms begin with the same set of governing equations describing the motion of the fluid and solid, as well as their interaction at the interface, but differ in the way they are solved. Monolithic schemes [6,7,24,30,32,37,42,45] solve the governing equations in one, fully-coupled, algebraic system, with implicitly imposed interface conditions. While in this way the fluid and structure remain strongly-coupled, the large system may likely become ill-conditioned and require specially designed preconditioners. On the other hand, partitioned methods [2,4,5,10,11,23,25–27,35,40,41,43,44]

Published online: 21 May 2021

use separate solvers for the fluid and structure sub-problems while enforcing coupling at the interface using a variety of potential boundary conditions, e.g. Dirichlet, Neumann, and Robin. In this way, each sub-problem has fewer unknowns and is better conditioned. However, stability issues often arise as a result of the coupling at the interface unless the design and implementation of a partitioned scheme is carefully developed.

Furthering the varying difficulties that arise amongst partitioned methods, certain physical factors play another role in making FSI problems especially challenging to solve. One such instance occurs in hemodynamics, where the structure and fluid densities are comparable, jeopardizing the stability due to *the added mass effect* [19]. In the case of thin structures, enforcing the structure's mass in the fluid problem is successfully done using different Robin boundary conditions on the interface [10,26,40,44]. However, such approaches cannot be directly applied when the dimension of the structure is the same as that of the fluid, i.e., in case of thick structures.

Whenever these added mass effect scenarios occur in FSI cases with thick structures, explicit Dirichlet–Neumann approaches are notorious for falling short because they are proven to be unconditionally unstable [19]. Even when sub-iterations are implemented in these cases in order to enforce stability (resulting in strongly-coupled partitioned schemes), convergence issues still arise. Hence, alternative options are to use the Robin–Dirichlet, Robin–Neumann, and Robin–Robin types of boundary conditions to be implemented on the fluid–structure interface [1,2,22,31,43]. These have been intensively analyzed for their efficacy in maintaining stability and convergence, and therefore widely used in different applications. We also mention the fictitious-pressure and fictitious-mass strongly-coupled algorithms proposed in [3,49], in which the added mass effect is accounted for by incorporating additional terms into governing equations.

When FSI problems with thick structures are solved using partitioned methods without sub-iterations, sub-optimal convergence in time may become an issue as seen in [10,13,15,28,46]. In particular, a partitioned, loosely-coupled scheme based on the Nitsche's penalty method was proposed in [15,17], where some interface terms were time-lagged in order to decouple the fluid and structure sub-problems. The scheme is proved to be stable under a CFL condition if a weakly consistent stabilization term that includes pressure variations at the interface is added. It was shown that the rate of convergence in time is $\mathcal{O}(\tau^{\frac{1}{2}})$, which was then corrected to obtain $\mathcal{O}(\tau)$ by proposing a few defect-correction sub-iterations. A non-iterative, Robin–Neumann partitioned scheme based on an interface operator accounting for the solid inertial effects within the fluid, has been proposed in [28]. The scheme has been analyzed on a linear FSI problem and shown to be stable under a time-step condition. However, a time step $\tau = \mathcal{O}(h^{\frac{3}{2}})$, where $h$ is the mesh size, is needed to achieve a first-order accuracy.

An alternative class of Added-Mass Partitioned algorithms has also been developed in [4,5,47]. A non-iterative, partitioned algorithm for FSI with thick structures was first proposed in [4]. It was shown that the algorithm is stable under a condition on the time step, which depends on the structure parameters. Although the authors do not derive the convergence rates, their numerical results indicate that the scheme is second-order accurate in time. In [47], the previously developed algorithms have been extended to finite deformations, and the explicit fluid solver was replaced by a fractional-step implicit-explicit scheme. We also mention an explicit Robin–Neumann scheme recently proposed and analyzed in [33], where the dependance of the stability of the method on the interface parameter in the Robin condition was studied. Furthermore, the stability of the method was analyzed on a model problem, and sufficient conditions for instability and stability were found. In our previous work [8], using the operator splitting approach, we developed a partitioned scheme for FSI with a thick, linearly viscoelastic structure. However, the assumption that the structure is viscoelastic was necessary in the derivation of the scheme, and the solid viscosity was solved implicitly with the fluid problem. Furthermore, the scheme was shown to be stable only under a condition on the time step [10]. More recently, we proposed a loosely-coupled method for FSI with thick structures [46] based on Robin coupling conditions, similar to a parallel work by Burman et al [14]. We proved that the method is unconditionally stable on a moving domain FSI problem using energy estimates. However, the method is shown to be only $\mathcal{O}(\tau^{\frac{1}{2}})$ in time [13,46].

In this paper, we are interested in solving FSI problems with thick, elastic structures and with a particular interest in applications with similar fluid and solid densities. The time dependent Stokes equations are used to describe the incompressible, viscous fluid, and the linearly elastic equations are employed for the solid. We propose a novel partitioned, strongly-coupled scheme, where the interface conditions are enforced with the use of Robin coupling conditions, similar as in [14,16,46]. These conditions are obtained by linearly combining the kinematic (Dirichlet) and dynamic (Neumann) interface conditions, along with the use of a combination parameter, $\alpha$, whose purpose is to dictate the emphasis on either the kinematic or dynamic condition. The time discretization is based on the one-legged '$\theta$-like' method proposed by Cauchy [18]. This family of methods, parametrized by $\theta$, is B-stable for any $\theta \in [\frac{1}{2}, 1]$ and second-order accurate for $\theta = \frac{1}{2} + \mathcal{O}(\tau)$. We note that $\theta = \frac{1}{2}$ corresponds to the midpoint rule.

In this work, similarly as in [12], we refactorize the Cauchy's method by writing it as sequential Backward Euler (BE)–Forward Euler (FE) problems. This results in first solving a partitioned scheme on $[t^n, t^{n+\theta}]$ discretized using the Backward Euler method in which we sub-iterate the fluid and structure sub-problems until convergence. Then, the variables are linearly extrapolated, equivalent to solving the Forward Euler problems on $[t^{n+\theta}, t^{n+1}]$. The partitioned scheme solved in the BE step is based on the loosely-coupled scheme presented in [14,16,46]. Therefore, the proposed method can be seen as its second-order extension (when $\theta = \frac{1}{2}$). We prove that the sub-iterative process in the proposed method is convergent and that the method is stable provided $\theta \in [\frac{1}{2}, 1]$. We also present an extension of our method to model a moving domain FSI, where the fluid is described using the Navier–Stokes equations in the Arbitrary Lagrangian-Eulerian (ALE) form.

The promising theoretical results are further illustrated in numerical examples, where the finite element method is used to discretize the problem in space. The first example uses the method of manufactured solutions to investigate convergence rates across varying values of the combination parameter, $\alpha$, used in the derivation of the Robin coupling condition, a parameter $\theta$, used in the time discretization, and the tolerance, $\epsilon$, used to control the sub-iterative procedure. The examples successfully meet, and in some cases exceed, the expectations of the second-order convergence in time. We also compare the average number of sub-iterations across multiple sub-iterative methods to our novel scheme in order to illustrate the reduced computational cost of our iterative approach. In particular, we show that the proposed method requires significantly fewer sub-iterations than the aforementioned Robin–Neumann and Robin–Robin methods. In the second numerical example, we consider a moving domain benchmark problem describing the flow in a two-dimensional channel with parameters similar to that of blood flow in order to show a comparison of the our method with the loosely-coupled scheme presented in [14,16,46].

The outline of this paper is as follows: We define the problem in Sect. 2 and elaborate upon our novel numerical method in Sect. 3. Convergence of the iterative procedure is analyzed and proven in Sect. 4, following up with the stability analysis in Sect. 5. Numerical examples are presented in Sect. 6. Section 7 highlights the conclusions of the main topics and results presented in this paper.

## 2. Problem Description

We consider the interaction between an incompressible, viscous fluid and a linearly elastic structure. The fluid domain is denoted by $\Omega_F$ and the structure domain by $\Omega_S$. We assume that $\Omega_F, \Omega_S \subset \mathbb{R}^d, d = 2, 3$ are open, smooth sets of the same dimension, and that the fluid–structure interface $\Gamma$ is the common boundary between the two domains, i.e. $\partial\Omega_F \cap \partial\Omega_S = \varnothing, \partial\bar{\Omega}_F \cap \partial\bar{\Omega}_S = \Gamma$, (see Fig. 1). The fluid inlet and outlet boundaries are designated by $\Gamma_F^{in}$ and $\Gamma_F^{out}$, respectively, the solid inlet and outlet boundaries by $\Gamma_S^{in}$ and $\Gamma_S^{out}$, respectively, and the external solid boundary by $\Gamma_S^{ext}$. Therefore, $\partial\Omega_F = \Gamma_F^{in} \cup \Gamma_F^{out} \cup \Gamma$ and $\partial\Omega_S = \Gamma_S^{in} \cup \Gamma_S^{out} \cup \Gamma_S^{ext} \cup \Gamma$. In the following, similarly as in [10,13–15,28], we assume that the structure deformation is infinitesimal, that fluid–structure interaction is linear, and that the fluid domain does not change.

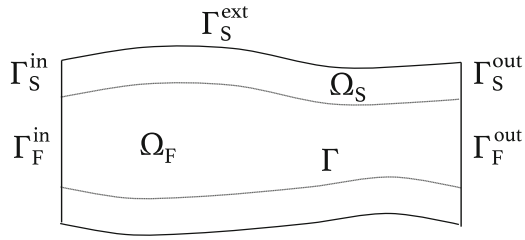


FIG. 1. Fluid domain $\Omega_F$ and structure domain $\Omega_S$, separated by a common interface $\Gamma$

To model the fluid flow, we use the time dependent Stokes equations, given as follows:

$$\rho_F \partial_t \boldsymbol{u} = \nabla \cdot \boldsymbol{\sigma}_F(\boldsymbol{u}, p) + \boldsymbol{f}_F \qquad \text{in } \Omega_F \times (0,T), \tag{2.1a}$$

$$\nabla \cdot \boldsymbol{u} = 0 \qquad \text{in } \Omega_F \times (0,T), \tag{2.1b}$$

where $\boldsymbol{u}$ is the fluid velocity, $\rho_F$ is fluid density, $\boldsymbol{\sigma}_F$ is the fluid stress tensor and $\boldsymbol{f}_F$ is the forcing term. For a Newtonian fluid, the stress tensor is given by $\boldsymbol{\sigma}_F(\boldsymbol{u}, p) = -p\boldsymbol{I} + 2\mu_F \boldsymbol{D}(\boldsymbol{u})$, where $p$ is the fluid pressure, $\mu_F$ is the fluid viscosity and $\boldsymbol{D}(\boldsymbol{u}) = (\nabla \boldsymbol{u} + (\nabla \boldsymbol{u})^T)/2$ is the strain rate tensor. At the inlet and outlet sections we prescribe Neumann boundary conditions:

$$\boldsymbol{\sigma}_F \boldsymbol{n}_F = -p_{in}(t)\boldsymbol{n}_F \qquad \text{on } \Gamma_F^{in} \times (0,T), \tag{2.2a}$$

$$\boldsymbol{\sigma}_F \boldsymbol{n}_F = -p_{out}(t)\boldsymbol{n}_F \qquad \text{on } \Gamma_F^{out} \times (0,T), \tag{2.2b}$$

where $\boldsymbol{n}_F$ is the outward unit normal to the fluid domain.

To model the elastic structure, we use the elastodynamics equations written in the first order form as

$$\rho_S \partial_t \boldsymbol{\xi} = \nabla \cdot \boldsymbol{\sigma}_S(\boldsymbol{\eta}) \qquad \text{in } \Omega_S \times (0,T), \tag{2.3a}$$

$$\partial_t \boldsymbol{\eta} = \boldsymbol{\xi} \qquad \text{in } \Omega_S \times (0,T), \tag{2.3b}$$

where $\boldsymbol{\eta}$ is the structure displacement, $\boldsymbol{\xi}$ is the structure velocity, $\rho_S$ is the structure density and $\boldsymbol{\sigma}_S$ is the solid Cauchy stress tensor. To describe the elastic material, we use the Saint Venant–Kirchhoff model, given as

$$\boldsymbol{\sigma}_S(\boldsymbol{\eta}) = 2\mu_S \boldsymbol{D}(\boldsymbol{\eta}) + \lambda_S (\nabla \cdot \boldsymbol{\eta}) \boldsymbol{I},$$

where $\mu_S$ and $\lambda_S$ are Lamé constants. We define a norm associated with the structure elastic energy as

$$\|\boldsymbol{\eta}\|_S^2 = 2\mu_S \|\boldsymbol{D}(\boldsymbol{\eta})\|_{L^2(\Omega_S)}^2 + \lambda_S \|\nabla \cdot \boldsymbol{\eta}\|_{L^2(\Omega_S)}^2. \tag{2.4}$$

The structure is assumed to be fixed at the inlet and outlet boundaries:

$$\boldsymbol{\eta} = 0 \quad \text{on } \Gamma_S^{in} \cup \Gamma_S^{out} \times (0,T), \tag{2.5}$$

and at the external structure boundary, $\Gamma_S^{ext}$, we impose:

$$\boldsymbol{\sigma}_S \boldsymbol{n}_S = 0 \quad \text{on } \Gamma_S^{ext} \times (0,T), \tag{2.6}$$

where $\boldsymbol{n}_S$ is the outward normal to the structure domain.

To couple the fluid and structure sub-problems, we prescribe the kinematic and dynamic coupling conditions [9,39], given as follows:

*Kinematic (no-slip) coupling condition* describes the continuity of velocity at the fluid–structure interface:

$$\boldsymbol{u} = \boldsymbol{\xi} \quad \text{on } \Gamma \times (0,T), \tag{2.7}$$

*Dynamic coupling condition* describes the continuity of stresses at the fluid–structure interface:

$$\boldsymbol{\sigma}_F \boldsymbol{n}_F + \boldsymbol{\sigma}_S \boldsymbol{n}_S = 0 \ \text{ on } \Gamma \times (0,T). \tag{2.8}$$

Initially, the fluid and structure are assumed to be at rest:

$$\boldsymbol{u} = 0 \quad \text{in } \Omega_F, \quad \boldsymbol{\eta} = 0, \ \boldsymbol{\xi} = 0 \quad \text{in } \Omega_S \quad \text{at } t = 0. \tag{2.9}$$

## 3. Numerical Method

Let $t^n = n\tau$ for $n = 0, \ldots, N$, where $\tau$ denotes the time step, and $t^{n+\theta} = t^n + \theta\tau$, for any $\theta \in [0, 1]$ and for all $n \geq 0$. Let $z^n$ denote the approximation of a time-dependent function $z$ at time level $t^n$. The proposed algorithm is based on the refactorization of the Cauchy's one-legged '$\theta$-like' method. In particular, for an initial value problem $y' = f(t, y(t))$, the Cauchy's one-legged '$\theta$-like' method is given as

$$\frac{y^{n+1} - y^n}{\tau} = f(t^{n+\theta}, y^{n+\theta}), \tag{3.1}$$

for $\theta \in [0, 1]$, where $y^{n+\theta} = \theta y^{n+1} + (1 - \theta)y^n$. We note that this method is a one-legged version of the 'classical' $\theta$-method

$$\frac{y^{n+1} - y^n}{\tau} = \theta f(t^{n+1}, y^{n+1}) + (1 - \theta) f(t^n, y^n)$$

analyzed in [34]. In the linear case both methods are the same, just as the trapezoidal and midpoint rule coincide, when one analyzes the A-stability property. For fully nonlinear cases, the methods have different behaviors, where the one-legged 'Cauchy' method is stable, unlike the $\theta$-method [21,48].

The Cauchy's method (3.1) can be solved in the BE-FE fashion [12] as

$$\text{BE:} \quad \frac{y^{n+\theta} - y^n}{\theta\tau} = f(t^{n+\theta}, y^{n+\theta}),$$
$$\text{FE:} \quad \frac{y^{n+1} - y^{n+\theta}}{(1 - \theta)\tau} = f(t^{n+\theta}, y^{n+\theta}).$$

The FE problem can also be written as a linear extrapolation given by

$$y^{n+1} = \frac{1}{\theta} y^{n+\theta} - \left(\frac{1}{\theta} - 1\right) y^n.$$

Using this approach, the main computational load of the algorithm is related to the computation of the BE steps, while computationally inexpensive linear extrapolations increase the accuracy of the scheme. We note that the case when $\theta = \frac{1}{2}$ corresponds to the midpoint rule, and it generally differs from the Crank-Nicolson method which is based on the trapezoidal rule [20,38].

The 'classical' $\theta$-method can be refactorized in a similar way as a FE-BE sequence. However, we use the Cauchy method since for $\theta = \frac{1}{2}$, we have a method that is B-stable even for variable steps [12], and the constant in the local truncation error (1/24) is half the size of the constant corresponding to the trapezoidal rule (-1/12).

The BE step of the proposed algorithm is obtained by sub-iterating the loosely-coupled scheme used in [14,16,46]. In particular, the method used in [14,16,46] is based on the Robin boundary conditions given as

$$\alpha\boldsymbol{\xi}^{n+1} + \boldsymbol{\sigma}_S^{n+1}\boldsymbol{n}_S = \alpha\boldsymbol{u}^n - \boldsymbol{\sigma}_F^n\boldsymbol{n}_F \quad \text{on } \Gamma \times (0, T), \tag{3.2}$$
$$\alpha\boldsymbol{\xi}^{n+1} - \boldsymbol{\sigma}_F^{n+1}\boldsymbol{n}_F = \alpha\boldsymbol{u}^{n+1} - \boldsymbol{\sigma}_F^n\boldsymbol{n}_F \quad \text{on } \Gamma \times (0, T), \tag{3.3}$$

where $\alpha > 0$ is a combination parameter. Condition (3.3) was obtained by multiplying (2.7) by $\alpha$ and adding the normal fluid stress to both sides of the equation. After time discretization, the two normal stresses were evaluated at different time levels. Condition (3.2) was obtained by multiplying (2.7) by $\alpha$ and adding it to (2.8).

Condition (3.2) is used as a Robin boundary condition for the structure sub-problem, and condition (3.3) is used as a Robin boundary condition for the fluid problem. We note that the difference between these coupling conditions and the ones used in the classical Robin–Robin method is in the second equation where the fluid normal stress is used twice, at different time levels. Due to this change, the method is unconditionally stable without requiring sub-iterations between the fluid and structure sub-problems [46]. However, it was noted that the method is sub-optimally, $\mathcal{O}(\tau^{\frac{1}{2}})$, accurate [14,46]. Hence, we propose to improve the accuracy by sub-iterating the fluid and solid sub-problems, combined

with an extrapolation step after the convergence is obtained, which for $\theta = \frac{1}{2}$ give second-order accuracy. Conditions (3.2)-(3.3) are adjusted so that the data taken from the previous time step is now taken from the previous sub-iteration. In particular, we use the following Robin boundary conditions

$$\alpha\boldsymbol{\xi}^{n+\theta}_{(\kappa+1)} + \boldsymbol{\sigma}^{n+\theta}_{S,(\kappa+1)}\boldsymbol{n}_S = \alpha\boldsymbol{u}^{n+\theta}_{(\kappa)} - \boldsymbol{\sigma}^{n+\theta}_{F,(\kappa)}\boldsymbol{n}_F \ \text{ on } \Gamma\times(0,T), \tag{3.4}$$

$$\alpha\boldsymbol{\xi}^{n+\theta}_{(\kappa+1)} - \boldsymbol{\sigma}^{n+\theta}_{F,(\kappa+1)}\boldsymbol{n}_F = \alpha\boldsymbol{u}^{n+\theta}_{(\kappa+1)} - \boldsymbol{\sigma}^{n+\theta}_{F,(\kappa)}\boldsymbol{n}_F \quad \text{on } \Gamma\times(0,T). \tag{3.5}$$

Once the sub-iterations converge, these conditions yield back the dynamic and kinematic condition at $t^{n+\theta}$, respectively.

The proposed partitioned numerical method is given in the following algorithm.

**Algorithm 1.** *Given $\boldsymbol{u}^0$ in $\Omega_F$, and $\boldsymbol{\eta}^0, \boldsymbol{\xi}^0$ in $\Omega_S$, we first need to compute $p^\theta, p^{1+\theta}, \boldsymbol{u}^1, \boldsymbol{u}^2$ in $\Omega_F$, and $\boldsymbol{\eta}^1, \boldsymbol{\eta}^2, \boldsymbol{\xi}^1, \boldsymbol{\xi}^2$ in $\Omega_S$ with a second-order method. A monolithic method could be used. Then, for all $n \geq 2$, compute the following steps:*

Step 1. *Set the initial guesses as the linearly extrapolated values:*

$$\boldsymbol{\eta}^{n+\theta}_{(0)} = \Big(1+\theta\Big)\boldsymbol{\eta}^n - \theta\boldsymbol{\eta}^{n-1},$$

*and similarly for $\boldsymbol{\xi}^{n+\theta}_{(0)}, \boldsymbol{u}^{n+\theta}_{(0)}$. The pressure initial guess is defined as*

$$p^{n+\theta}_{(0)} = (1+\tau)p^{n-1+\theta} - \tau p^{n-2+\theta}.$$

*For $\kappa \geq 0$, compute until convergence the following* **Backward Euler** *partitioned problem:*

$$\text{Solid}: \begin{cases} \dfrac{\boldsymbol{\eta}^{n+\theta}_{(\kappa+1)} - \boldsymbol{\eta}^n}{\theta\tau} = \boldsymbol{\xi}^{n+\theta}_{(\kappa+1)} & \text{in } \Omega_S, \quad (3.6a)\\ \rho_S \dfrac{\boldsymbol{\xi}^{n+\theta}_{(\kappa+1)} - \boldsymbol{\xi}^n}{\theta\tau} = \nabla\cdot\boldsymbol{\sigma}_S(\boldsymbol{\eta}^{n+\theta}_{(\kappa+1)}) & \text{in } \Omega_S, \quad (3.6b)\\ \alpha\boldsymbol{\xi}^{n+\theta}_{(\kappa+1)} + \boldsymbol{\sigma}_S(\boldsymbol{\eta}^{n+\theta}_{(\kappa+1)})\boldsymbol{n}_S = \alpha\boldsymbol{u}^{n+\theta}_{(\kappa)} & \\ \quad -\boldsymbol{\sigma}_F(\boldsymbol{u}^{n+\theta}_{(\kappa)}, p^{n+\theta}_{(\kappa)})\boldsymbol{n}_F & \text{on } \Gamma, \quad (3.6c)\\ \boldsymbol{\eta}^{n+\theta}_{(\kappa+1)} = 0 & \text{on } \Gamma^{in}_S \cup \Gamma^{out}_S, \quad (3.6d)\\ \boldsymbol{\sigma}_S(\boldsymbol{\eta}^{n+\theta}_{(\kappa+1)})\boldsymbol{n}_S = 0 & \text{on } \Gamma^{ext}_S, \quad (3.6e) \end{cases}$$

$$\text{Fluid:} \begin{cases} \rho_F \dfrac{\boldsymbol{u}^{n+\theta}_{(\kappa+1)} - \boldsymbol{u}^n}{\theta\tau} - \nabla\cdot\boldsymbol{\sigma}_F(\boldsymbol{u}^{n+\theta}_{(\kappa+1)}, p^{n+\theta}_{(\kappa+1)}) & \quad (3.7a)\\ \quad = \boldsymbol{f}_F(t^{n+\theta}) & \text{in } \Omega_F, \quad (3.7b)\\ \nabla\cdot\boldsymbol{u}^{n+\theta}_{(\kappa+1)} = 0 & \text{in } \Omega_F, \quad (3.7c)\\ \alpha\boldsymbol{u}^{n+\theta}_{(\kappa+1)} - \boldsymbol{\sigma}_F(\boldsymbol{u}^{n+\theta}_{(\kappa)}, p^{n+\theta}_{(\kappa)})\boldsymbol{n}_F = \alpha\boldsymbol{\xi}^{n+\theta}_{(\kappa+1)} & \\ \quad -\boldsymbol{\sigma}_F(\boldsymbol{u}^{n+\theta}_{(\kappa+1)}, p^{n+\theta}_{(\kappa+1)})\boldsymbol{n}_F & \text{on } \Gamma, \quad (3.7d)\\ \boldsymbol{\sigma}_F(\boldsymbol{u}^{n+\theta}_{(\kappa+1)}, p^{n+\theta}_{(\kappa+1)})\boldsymbol{n}_F = -p_{in}(t^{n+\theta})\boldsymbol{n}_F & \text{on } \Gamma^{in}_F, \quad (3.7e)\\ \boldsymbol{\sigma}_F(\boldsymbol{u}^{n+\theta}_{(\kappa+1)}, p^{n+\theta}_{(\kappa+1)})\boldsymbol{n}_F = -p_{out}(t^{n+\theta})\boldsymbol{n}_F & \text{on } \Gamma^{out}_F. \quad (3.7f) \end{cases}$$

*The converged solutions,*

$$\boldsymbol{\eta}^{n+\theta}_{(\kappa)}, \boldsymbol{\xi}^{n+\theta}_{(\kappa)}, \boldsymbol{u}^{n+\theta}_{(\kappa)}, p^{n+\theta}_{(\kappa)} \xrightarrow{\kappa\to\infty} \boldsymbol{\eta}^{n+\theta}, \boldsymbol{\xi}^{n+\theta}, \boldsymbol{u}^{n+\theta}, p^{n+\theta},$$

*then satisfy:*

$$\text{Solid:}\begin{cases}\dfrac{\boldsymbol{\eta}^{n+\theta}-\boldsymbol{\eta}^{n}}{\theta\tau}=\boldsymbol{\xi}^{n+\theta} & \text{in } \Omega_S, \quad (3.8a)\\ \rho_S\dfrac{\boldsymbol{\xi}^{n+\theta}-\boldsymbol{\xi}^{n}}{\theta\tau}=\nabla\cdot\boldsymbol{\sigma}_S(\boldsymbol{\eta}^{n+\theta}) & \text{in } \Omega_S, \quad (3.8b)\\ \boldsymbol{\sigma}_S(\boldsymbol{\eta}^{n+\theta})\boldsymbol{n}_S=-\boldsymbol{\sigma}_F(\boldsymbol{u}^{n+\theta},p^{n+\theta})\boldsymbol{n}_F & \text{on } \Gamma, \quad (3.8c)\\ \boldsymbol{\eta}^{n+\theta}=0 & \text{on } \Gamma_S^{in}\cup\Gamma_S^{out}, \quad (3.8d)\\ \boldsymbol{\sigma}_S(\boldsymbol{\eta}^{n+\theta})\boldsymbol{n}_S=0 & \text{on } \Gamma_S^{ext}, \quad (3.8e)\end{cases}$$

$$\text{Fluid:}\begin{cases}\rho_F\dfrac{\boldsymbol{u}^{n+\theta}-\boldsymbol{u}^{n}}{\theta\tau}-\nabla\cdot\boldsymbol{\sigma}_F(\boldsymbol{u}^{n+\theta},p^{n+\theta})\\ \quad=\boldsymbol{f}_F(t^{n+\theta}) & \text{in } \Omega_F, \quad (3.9a)\\ \nabla\cdot\boldsymbol{u}^{n+\theta}=0 & \text{in } \Omega_F, \quad (3.9b)\\ \boldsymbol{u}^{n+\theta}=\boldsymbol{\xi}^{n+\theta} & \text{on } \Gamma. \quad (3.9c)\\ \boldsymbol{\sigma}_F(\boldsymbol{u}^{n+\theta},p^{n+\theta})\boldsymbol{n}_F=-p_{in}(t^{n+\theta})\boldsymbol{n}_F & \text{on } \Gamma_F^{in}, \quad (3.9d)\\ \boldsymbol{\sigma}_F(\boldsymbol{u}^{n+\theta},p^{n+\theta})\boldsymbol{n}_F=-p_{out}(t^{n+\theta})\boldsymbol{n}_F & \text{on } \Gamma_F^{out}. \quad (3.9e)\end{cases}$$

Step 2. *Now evaluate the following (equivalent to solving* **Forward Euler** *problems):*

$$\text{Solid:}\begin{cases}\boldsymbol{\eta}^{n+1}=\dfrac{1}{\theta}\boldsymbol{\eta}^{n+\theta}-\dfrac{1-\theta}{\theta}\boldsymbol{\eta}^{n} & \text{in } \Omega_S, \quad (3.10a)\\ \boldsymbol{\xi}^{n+1}=\dfrac{1}{\theta}\boldsymbol{\xi}^{n+\theta}-\dfrac{1-\theta}{\theta}\boldsymbol{\xi}^{n} & \text{in } \Omega_S, \quad (3.10b)\end{cases}$$

$$\text{Fluid:}\begin{cases}\boldsymbol{u}^{n+1}=\dfrac{1}{\theta}\boldsymbol{u}^{n+\theta}-\dfrac{1-\theta}{\theta}\boldsymbol{u}^{n} & \text{in } \Omega_F, \quad (3.11a)\end{cases}$$

Set $n=n+1$, and go back to Step 1.

*Remark 1.* From a computational viewpoint, the bulk of the work in Algorithm 1 is performed in the BE steps (3.6)–(3.7), as the FE steps (3.10)–(3.11), written as linear extrapolations, act as time-filters. For the theoretical argumentation, we will use their equivalent FE form:

$$\text{Solid:}\begin{cases}\dfrac{\boldsymbol{\eta}^{n+1}-\boldsymbol{\eta}^{n+\theta}}{(1-\theta)\tau}=\boldsymbol{\xi}^{n+\theta} & \text{in } \Omega_S, \quad (3.12a)\\ \rho_S\dfrac{\boldsymbol{\xi}^{n+1}-\boldsymbol{\xi}^{n+\theta}}{(1-\theta)\tau}=\nabla\cdot\boldsymbol{\sigma}_S(\boldsymbol{\eta}^{n+\theta}) & \text{in } \Omega_S, \quad (3.12b)\end{cases}$$

$$\text{Fluid:}\begin{cases}\rho_F\dfrac{\boldsymbol{u}^{n+1}-\boldsymbol{u}^{n+\theta}}{(1-\theta)\tau}-\nabla\cdot\boldsymbol{\sigma}(\boldsymbol{u}^{n+\theta},p^{n+\theta})\\ \quad=\boldsymbol{f}_F(t^{n+\theta}) & \text{in } \Omega_F. \quad (3.13)\end{cases}$$

*Remark 2.* We note that the proposed method is similar to the algorithm developed in [15,16], which was obtained by enforcing coupling conditions using Nitsche's penalty method. In particular, an explicit method was proposed in [15] based on the Nitsche's method, which was shown to be sub-optimally convergent in time. The incomplete version of that method, without stabilizing terms that were added in [15], is equivalent to the loosely-coupled Robin–Robin scheme used in [14,16,46]. To obtain convergence rate $\mathcal{O}(\tau)$, the authors in [15] suggested to perform a few defect-correction iterations in the similar way as in the BE step of Algorithm 1. However, the method in [15] contains additional terms that come from the application of Nitsche's method. Furthermore, no second-order extensions were considered in [15].

*Remark 3.* The classical strongly coupled Robin–Robin methods typically use the Robin boundary conditions obtained with two different combination parameters, $\alpha_F$ and $\alpha_S$ [1,2]. However, we consider a single parameter $\alpha = \alpha_F = \alpha_S$, which is needed in order to obtain unconditional stability, both in [14,46] and this work.

## 4. Convergence of the Partitioned Iterative Method

In this section, we show that the iterative method defined by (3.6)–(3.7) converges. In the following, we will use the polarized identity given by:

$$2(a-c)b = a^2 - c^2 - (a-b)^2 + (b-c)^2 \tag{4.1}$$

**Theorem 1.** *The sequences* $\boldsymbol{u}_{(\kappa)}^{n+\theta}, \boldsymbol{\eta}_{(\kappa)}^{n+\theta}, \boldsymbol{\xi}_{(\kappa)}^{n+\theta}$ *generated by the iterations (3.6)–(3.7) converge as* $\kappa \to \infty$*:*

$$\begin{aligned}
&\boldsymbol{u}_{(\kappa)}^{n+\theta} \longrightarrow \boldsymbol{u}^{n+\theta} \quad \text{in } \ell^\infty(H^1(\Gamma)) \cap \ell^2(L^2(\Gamma)) \cap \ell^2(H^1(\Omega_F)),\\
&\boldsymbol{\eta}_{(\kappa)}^{n+\theta} \longrightarrow \boldsymbol{\eta}^{n+\theta} \quad \text{in } \ell^2(S),\\
&\boldsymbol{\xi}_{(\kappa)}^{n+\theta} \longrightarrow \boldsymbol{\xi}^{n+\theta} \quad \text{in } \ell^2(L^2(\Omega_S)) \cap \ell^2(L^2(\Gamma)).
\end{aligned}$$

*Proof.* We begin by subtracting (3.6)–(3.7) at iteration $\kappa$ from the same equations at iteration $\kappa+1$. Using notation

$$\begin{aligned}
\boldsymbol{\delta}_{\kappa+1}^{\eta} &= \boldsymbol{\eta}_{(\kappa+1)}^{n+\theta} - \boldsymbol{\eta}_{(\kappa)}^{n+\theta},\\
\boldsymbol{\delta}_{\kappa+1}^{\xi} &= \boldsymbol{\xi}_{(\kappa+1)}^{n+\theta} - \boldsymbol{\xi}_{(\kappa)}^{n+\theta},\\
\boldsymbol{\delta}_{\kappa+1}^{u} &= \boldsymbol{u}_{(\kappa+1)}^{n+\theta} - \boldsymbol{u}_{(\kappa)}^{n+\theta},\\
\delta_{\kappa+1}^{p} &= p_{(\kappa+1)}^{n+\theta} - p_{(\kappa)}^{n+\theta},
\end{aligned} \tag{4.2}$$

we obtain the following:

$$\text{Solid:}\begin{cases}
\dfrac{\boldsymbol{\delta}_{\kappa+1}^{\eta}}{\theta\tau} = \boldsymbol{\delta}_{\kappa+1}^{\xi} & \text{in } \Omega_S, \quad (4.3a)\\
\rho_S \dfrac{\boldsymbol{\delta}_{\kappa+1}^{\xi}}{\theta\tau} = \nabla\cdot\boldsymbol{\sigma}_S(\boldsymbol{\delta}_{\kappa+1}^{\eta}) & \text{in } \Omega_S, \quad (4.3b)\\
\alpha\boldsymbol{\delta}_{\kappa+1}^{\xi} + \boldsymbol{\sigma}_S(\boldsymbol{\delta}_{\kappa+1}^{\eta})\boldsymbol{n}_S = \alpha\boldsymbol{\delta}_{\kappa}^{u} & \\
\quad -\boldsymbol{\sigma}_F(\boldsymbol{\delta}_{\kappa}^{u}, \delta_{\kappa}^{p})\boldsymbol{n}_F & \text{on } \Gamma, \quad (4.3c)\\
\boldsymbol{\delta}_{\kappa+1}^{\eta} = 0 & \text{on } \Gamma_S^{in}\cup\Gamma_S^{out}, \quad (4.3d)\\
\boldsymbol{\sigma}_S(\boldsymbol{\delta}_{\kappa+1}^{\eta})\boldsymbol{n}_S = 0 & \text{on } \Gamma_S^{ext}, \quad (4.3e)
\end{cases}$$

$$\text{Fluid:}\begin{cases}
\rho_F\dfrac{\boldsymbol{\delta}_{\kappa+1}^{u}}{\theta\tau} - \nabla\cdot\boldsymbol{\sigma}_F(\boldsymbol{\delta}_{\kappa+1}^{u}, \delta_{\kappa+1}^{p}) = 0 & \text{in } \Omega_F, \quad (4.4a)\\
\nabla\cdot\boldsymbol{\delta}_{\kappa+1}^{u} = 0 & \text{in } \Omega_F, \quad (4.4b)\\
\alpha\boldsymbol{\delta}_{\kappa+1}^{u} - \boldsymbol{\sigma}_F(\boldsymbol{\delta}_{\kappa}^{u}, \delta_{\kappa}^{p})\boldsymbol{n}_F & \\
\quad = \alpha\boldsymbol{\delta}_{\kappa+1}^{\xi} - \boldsymbol{\sigma}_F(\boldsymbol{\delta}_{\kappa+1}^{u}, \delta_{\kappa+1}^{p})\boldsymbol{n}_F & \text{on } \Gamma, \quad (4.4c)\\
\boldsymbol{\sigma}_F(\boldsymbol{\delta}_{\kappa+1}^{u}, \delta_{\kappa+1}^{p})\boldsymbol{n}_F = 0 & \text{on } \Gamma_F^{in}, \quad (4.4d)\\
\boldsymbol{\sigma}_F(\boldsymbol{\delta}_{\kappa+1}^{u}, \delta_{\kappa+1}^{p})\boldsymbol{n}_F = 0 & \text{on } \Gamma_F^{out}. \quad (4.4e)
\end{cases}$$

We multiply (4.3b) by $\boldsymbol{\delta}_{\kappa+1}^{\xi}$ and integrate over $\Omega_S$. Using (4.3a) and (2.4), we have:

$$0 = \frac{\rho_S}{\theta\tau}\left\|\boldsymbol{\delta}_{\kappa+1}^{\xi}\right\|_{L^2(\Omega_S)}^2 + \frac{1}{\theta\tau}\left\|\boldsymbol{\delta}_{\kappa+1}^{\eta}\right\|_S^2 - \int_\Gamma \boldsymbol{\sigma}_S(\boldsymbol{\delta}_{\kappa+1}^{\eta})\boldsymbol{n}_S\cdot\boldsymbol{\delta}_{\kappa+1}^{\xi}.$$

Using condition (4.3c) and identity (4.1), we have:

$$0 = \frac{\rho_S}{\theta\tau}\left\|\boldsymbol{\delta}^{\xi}_{\kappa+1}\right\|^2_{L^2(\Omega_S)} + \frac{1}{\theta\tau}\left\|\boldsymbol{\delta}^{\eta}_{\kappa+1}\right\|^2_{S} + \frac{\alpha}{2}\left\|\boldsymbol{\delta}^{\xi}_{\kappa+1}\right\|^2_{L^2(\Gamma)} - \frac{\alpha}{2}\left\|\boldsymbol{\delta}^{u}_{\kappa}\right\|^2_{L^2(\Gamma)} + \frac{\alpha}{2}\left\|\boldsymbol{\delta}^{\xi}_{\kappa+1} - \boldsymbol{\delta}^{u}_{\kappa}\right\|^2_{L^2(\Gamma)} + \int_{\Gamma}\boldsymbol{\sigma}_F(\boldsymbol{\delta}^{u}_{\kappa}, \delta^{p}_{\kappa})\boldsymbol{n}_F \cdot \boldsymbol{\delta}^{\xi}_{\kappa+1}. \tag{4.5}$$

We address the fluid in a similar manner. Multiplying (4.4a) by $\boldsymbol{\delta}^{u}_{\kappa+1}$, (4.4b) by $\boldsymbol{\delta}^{p}_{\kappa+1}$, integrating over $\Omega_F$ and adding the resulting equations together, we obtain:

$$0 = \frac{\rho_F}{\theta\tau}\left\|\boldsymbol{\delta}^{u}_{\kappa+1}\right\|^2_{L^2(\Omega_F)} + 2\mu_F\left\|\boldsymbol{D}(\boldsymbol{\delta}^{u}_{\kappa+1})\right\|^2_{L^2(\Omega_F)} - \int_{\Gamma}\boldsymbol{\sigma}_F(\boldsymbol{\delta}^{u}_{\kappa+1}, \delta^{p}_{\kappa+1})\boldsymbol{n}_F \cdot \boldsymbol{\delta}^{u}_{\kappa+1}.$$

Using Robin condition (4.4c) and identity (4.1), we have:

$$\begin{aligned} 0 = {} & \frac{\rho_F}{\theta\tau}\left\|\boldsymbol{\delta}^{u}_{\kappa+1}\right\|^2_{L^2(\Omega_F)} + 2\mu_F\left\|\boldsymbol{D}(\boldsymbol{\delta}^{u}_{\kappa+1})\right\|^2_{L^2(\Omega_F)} + \frac{\alpha}{2}\left\|\boldsymbol{\delta}^{u}_{\kappa+1}\right\|^2_{L^2(\Gamma)} \\ & - \frac{\alpha}{2}\left\|\boldsymbol{\delta}^{\xi}_{\kappa+1}\right\|^2_{L^2(\Gamma)} + \frac{\alpha}{2}\left\|\boldsymbol{\delta}^{u}_{\kappa+1} - \boldsymbol{\delta}^{\xi}_{\kappa+1}\right\|^2_{L^2(\Gamma)} \\ & - \int_{\Gamma}\boldsymbol{\sigma}_F(\boldsymbol{\delta}^{u}_{\kappa}, \delta^{p}_{\kappa})\boldsymbol{n}_F \cdot \boldsymbol{\delta}^{u}_{\kappa+1}. \end{aligned} \tag{4.6}$$

Combining structure (4.5) and fluid (4.6) estimates, we obtain:

$$\begin{aligned} 0 = {} & \frac{\rho_S}{\theta\tau}\left\|\boldsymbol{\delta}^{\xi}_{\kappa+1}\right\|^2_{L^2(\Omega_S)} + \frac{1}{\theta\tau}\left\|\boldsymbol{\delta}^{\eta}_{\kappa+1}\right\|^2_{S} + \frac{\rho_F}{\theta\tau}\left\|\boldsymbol{\delta}^{u}_{\kappa+1}\right\|^2_{L^2(\Omega_F)} \\ & + 2\mu_F\left\|\boldsymbol{D}(\boldsymbol{\delta}^{u}_{\kappa+1})\right\|^2_{L^2(\Omega_F)} + \frac{\alpha}{2}\left\|\boldsymbol{\delta}^{u}_{\kappa+1}\right\|^2_{L^2(\Gamma)} - \frac{\alpha}{2}\left\|\boldsymbol{\delta}^{u}_{\kappa}\right\|^2_{L^2(\Gamma)} \\ & + \frac{\alpha}{2}\left\|\boldsymbol{\delta}^{\xi}_{\kappa+1} - \boldsymbol{\delta}^{u}_{\kappa}\right\|^2_{L^2(\Gamma)} + \frac{\alpha}{2}\left\|\boldsymbol{\delta}^{u}_{\kappa+1} - \boldsymbol{\delta}^{\xi}_{\kappa+1}\right\|^2_{L^2(\Gamma)} \\ & + \int_{\Gamma}\boldsymbol{\sigma}_F(\boldsymbol{\delta}^{u}_{\kappa}, \delta^{p}_{\kappa})\boldsymbol{n}_F \cdot \left(\boldsymbol{\delta}^{\xi}_{\kappa+1} - \boldsymbol{\delta}^{u}_{\kappa+1}\right). \end{aligned} \tag{4.7}$$

Using (4.4c) and (4.1), the last term can be written as:

$$\begin{aligned} & \int_{\Gamma}\boldsymbol{\sigma}_F(\boldsymbol{\delta}^{u}_{\kappa}, \delta^{p}_{\kappa})\boldsymbol{n}_F \cdot \left(\boldsymbol{\delta}^{\xi}_{\kappa+1} - \boldsymbol{\delta}^{u}_{\kappa+1}\right) \\ & \quad = \frac{1}{2\alpha}\left\|\boldsymbol{\sigma}_F(\boldsymbol{\delta}^{u}_{\kappa+1}, \delta^{p}_{\kappa+1})\boldsymbol{n}_F\right\|^2_{L^2(\Gamma)} - \frac{1}{2\alpha}\left\|\boldsymbol{\sigma}_F(\boldsymbol{\delta}^{u}_{\kappa}, \delta^{p}_{\kappa})\boldsymbol{n}_F\right\|^2_{L^2(\Gamma)} \\ & \quad\quad - \frac{1}{2\alpha}\left\|\boldsymbol{\sigma}_F(\boldsymbol{\delta}^{u}_{\kappa+1}, \delta^{p}_{\kappa+1})\boldsymbol{n}_F - \boldsymbol{\sigma}_F(\boldsymbol{\delta}^{u}_{\kappa}, \delta^{p}_{\kappa})\boldsymbol{n}_F\right\|^2_{L^2(\Gamma)}. \end{aligned} \tag{4.8}$$

Using (4.4c) again, and combining (4.8) with (4.7), we obtain:

$$\begin{aligned} 0 = {} & \frac{\rho_S}{\theta\tau}\left\|\boldsymbol{\delta}^{\xi}_{\kappa+1}\right\|^2_{L^2(\Omega_S)} + \frac{1}{\theta\tau}\left\|\boldsymbol{\delta}^{\eta}_{\kappa+1}\right\|^2_{S} + \frac{\rho_F}{\theta\tau}\left\|\boldsymbol{\delta}^{u}_{\kappa+1}\right\|^2_{L^2(\Omega_F)} \\ & + 2\mu_F\left\|\boldsymbol{D}(\boldsymbol{\delta}^{u}_{\kappa+1})\right\|^2_{L^2(\Omega_F)} + \frac{\alpha}{2}\left\|\boldsymbol{\delta}^{u}_{\kappa+1}\right\|^2_{L^2(\Gamma)} - \frac{\alpha}{2}\left\|\boldsymbol{\delta}^{u}_{\kappa}\right\|^2_{L^2(\Gamma)} \\ & + \frac{\alpha}{2}\left\|\boldsymbol{\delta}^{\xi}_{\kappa+1} - \boldsymbol{\delta}^{u}_{\kappa}\right\|^2_{L^2(\Gamma)} + \frac{1}{2\alpha}\left\|\boldsymbol{\sigma}_F(\boldsymbol{\delta}^{u}_{\kappa+1}, \delta^{p}_{\kappa+1})\boldsymbol{n}_F\right\|^2_{L^2(\Gamma)} \\ & - \frac{1}{2\alpha}\left\|\boldsymbol{\sigma}_F(\boldsymbol{\delta}^{u}_{\kappa}, \delta^{p}_{\kappa})\boldsymbol{n}_F\right\|^2_{L^2(\Gamma)}. \end{aligned} \tag{4.9}$$

Summing from $\kappa = 1$ to $l-1$, we get:

$$\frac{\rho_S}{\theta\tau}\sum_{\kappa=1}^{l-1}\left\|\boldsymbol{\delta}^{\xi}_{\kappa+1}\right\|^2_{L^2(\Omega_S)} + \frac{1}{\theta\tau}\sum_{\kappa=1}^{l-1}\left\|\boldsymbol{\delta}^{\eta}_{\kappa+1}\right\|^2_{S} + \frac{\rho_F}{\theta\tau}\sum_{\kappa=1}^{l-1}\left\|\boldsymbol{\delta}^{u}_{\kappa+1}\right\|^2_{L^2(\Omega_F)}$$

$$+ 2\mu_F \sum_{\kappa=1}^{l-1} \left\| \boldsymbol{D}(\boldsymbol{\delta}^u_{\kappa+1}) \right\|^2_{L^2(\Omega_F)} + \frac{\alpha}{2} \sum_{\kappa=1}^{l-1} \left\| \boldsymbol{\delta}^{\xi}_{\kappa+1} - \boldsymbol{\delta}^u_{\kappa} \right\|^2_{L^2(\Gamma)}$$
$$+ \frac{\alpha}{2} \|\boldsymbol{\delta}^u_l\|^2_{L^2(\Gamma)} + \frac{1}{2\alpha} \|\boldsymbol{\sigma}_F(\boldsymbol{\delta}^u_l, \delta^p_l)\boldsymbol{n}_F\|^2_{L^2(\Gamma)}$$
$$= \frac{\alpha}{2} \|\boldsymbol{\delta}^u_1\|^2_{L^2(\Gamma)} + \frac{1}{2\alpha} \|\boldsymbol{\sigma}_F(\boldsymbol{\delta}^u_1, \delta^p_1)\boldsymbol{n}_F\|^2_{L^2(\Gamma)}. \tag{4.10}$$

Hence, $\boldsymbol{\eta}^{n+\theta}_{(\kappa)}$ and $\boldsymbol{\xi}^{n+\theta}_{(\kappa)}$, and $\boldsymbol{u}^{n+\theta}_{(\kappa)}$ are Cauchy sequences in $\ell^2(S), \ell^2(L^2(\Omega_S)) \cap \ell^2(L^2(\Gamma))$ and $\ell^\infty(H^1(\Gamma)) \cap \ell^2(L^2(\Gamma)) \cap \ell^2(H^1(\Omega_F))$, respectively. The completeness of the spaces implies the convergence of the iterations, completing the proof. □

## 5. Stability Analysis

In this section, we prove the stability of the partitioned method presented in Algorithm 1. In particular, we consider the scheme described by the BE steps (3.8)–(3.9) and FE steps (3.12)–(3.13). As noted in Remark 1, the FE steps are equivalent to linear extrapolations (3.10)–(3.11).

Let $\mathcal{E}^n$ denote the sum of the kinetic and elastic energy of the solid, and kinetic energy of the fluid, defined as:

$$\mathcal{E}^n = \frac{\rho_S}{2} \|\boldsymbol{\xi}^n\|^2_{L^2(\Omega_S)} + \frac{1}{2} \|\boldsymbol{\eta}^n\|^2_S + \frac{\rho_F}{2} \|\boldsymbol{u}^n\|^2_{L^2(\Omega_F)},$$

let $\mathcal{D}^n$ denote the fluid viscous dissipation, given by:

$$\mathcal{D}^n = \mu_F \tau \sum_{k=2}^{n-1} \|\boldsymbol{D}(\boldsymbol{u}^{k+\theta})\|^2_{L^2(\Omega_F)},$$

let $\mathcal{N}^n$ denote the terms present due to numerical dissipation:

$$\mathcal{N}^n = \frac{(2\theta-1)}{2\tau} \sum_{k=2}^{n-1} \left( \rho_S \left\| \boldsymbol{\xi}^{k+1} - \boldsymbol{\xi}^k \right\|^2_{L^2(\Omega_S)} + \left\| \boldsymbol{\eta}^{k+1} - \boldsymbol{\eta}^k \right\|^2_S \right)$$
$$+ \frac{\rho_F(2\theta-1)}{2\tau} \sum_{k=2}^{n-1} \|\boldsymbol{u}^{k+1} - \boldsymbol{u}^k\|^2_{L^2(\Omega_F)},$$

and let $\mathcal{F}^n$ denote the forcing terms:

$$\mathcal{F}^n = \frac{\tau}{\mu_F} \sum_{k=2}^{n-1} \left( C_1 \|\boldsymbol{f}_F(t^{k+\theta})\|^2_{L^2(\Omega_F)} + C_2 \|p_{in}(t^{k+\theta})\|^2_{L^2(\Gamma^{in}_F)} \right)$$
$$+ \frac{\tau}{\mu_F} \sum_{k=2}^{n-1} C_2 \|p_{out}(t^{k+\theta})\|^2_{L^2(\Gamma^{out}_F)}.$$

The stability result is given in the following theorem.

**Theorem 2.** *Let $\{(\boldsymbol{\xi}^n, \boldsymbol{\eta}^n, \boldsymbol{u}^n, p^n)\}_{2 \le n \le N}$ be the solution of Algorithm 1. Assume that $\theta \in [\frac{1}{2}, 1]$. Then, the following estimate holds:*

$$\mathcal{E}^N + \mathcal{D}^N + \mathcal{N}^N \le \mathcal{E}^2 + \mathcal{F}^N. \tag{5.1}$$

*Proof.* We multiply (3.8b) by $\theta\boldsymbol{\xi}^{n+\theta}$, integrate over $\Omega_S$, and use (3.8a) and (4.1), which yields:

$$0 = \frac{\rho_S}{2\tau} \left( \|\boldsymbol{\xi}^{n+\theta}\|^2_{L^2(\Omega_S)} - \|\boldsymbol{\xi}^n\|^2_{L^2(\Omega_S)} + \|\boldsymbol{\xi}^{n+\theta} - \boldsymbol{\xi}^n\|^2_{L^2(\Omega_S)} \right)$$
$$+ \frac{1}{2\tau} \left( \|\boldsymbol{\eta}^{n+\theta}\|^2_S - \|\boldsymbol{\eta}^n\|^2_S + \|\boldsymbol{\eta}^{n+\theta} - \boldsymbol{\eta}^n\|^2_S \right) - \theta \int_\Gamma \boldsymbol{\sigma}_S(\boldsymbol{\eta}^{n+\theta}) \boldsymbol{n}_S \boldsymbol{\xi}^{n+\theta}. \tag{5.2}$$

Similarly, we multiply (3.12b) by $(1-\theta)\boldsymbol{\xi}^{n+\theta}$, integrate over $\Omega_S$ and use (3.12a) and (4.1) in order to obtain:

$$\begin{aligned}0 = &\frac{\rho_S}{2\tau}\left(\|\boldsymbol{\xi}^{n+1}\|^2_{L^2(\Omega_S)} - \|\boldsymbol{\xi}^{n+\theta}\|^2_{L^2(\Omega_S)} - \|\boldsymbol{\xi}^{n+\theta} - \boldsymbol{\xi}^{n+1}\|^2_{L^2(\Omega_S)}\right)\\ &+ \frac{1}{2\tau}\left(\|\boldsymbol{\eta}^{n+1}\|^2_S - \|\boldsymbol{\eta}^{n+\theta}\|^2_S - \|\boldsymbol{\eta}^{n+\theta} - \boldsymbol{\eta}^{n+1}\|^2_S\right)\\ &- (1-\theta)\int_\Gamma \boldsymbol{\sigma}_S(\boldsymbol{\eta}^{n+\theta})\boldsymbol{n}_S \cdot \boldsymbol{\xi}^{n+\theta}.\end{aligned} \tag{5.3}$$

Adding (5.2) and (5.3), and using (3.8c), we have:

$$\begin{aligned}0 = &\frac{\rho_S}{2\tau}\left(\|\boldsymbol{\xi}^{n+1}\|^2_{L^2(\Omega_S)} - \|\boldsymbol{\xi}^{n}\|^2_{L^2(\Omega_S)} + \|\boldsymbol{\xi}^{n+\theta} - \boldsymbol{\xi}^{n}\|^2_{L^2(\Omega_S)}\right)\\ &- \frac{\rho_S}{2\tau}\|\boldsymbol{\xi}^{n+\theta} - \boldsymbol{\xi}^{n+1}\|^2_{L^2(\Omega_S)} + \frac{1}{2\tau}\left(\|\boldsymbol{\eta}^{n+1}\|^2_S - \|\boldsymbol{\eta}^{n}\|^2_S + \|\boldsymbol{\eta}^{n+\theta} - \boldsymbol{\eta}^{n}\|^2_S\right)\\ &- \frac{1}{2\tau}\|\boldsymbol{\eta}^{n+\theta} - \boldsymbol{\eta}^{n+1}\|^2_S + \int_\Gamma \boldsymbol{\sigma}_F(\boldsymbol{u}^{n+\theta}, p^{n+\theta})\boldsymbol{n}_F \cdot \boldsymbol{\xi}^{n+\theta}.\end{aligned} \tag{5.4}$$

Using (3.10b), we have:

$$\begin{aligned}&\|\boldsymbol{\xi}^{n+\theta} - \boldsymbol{\xi}^{n}\|^2_{L^2(\Omega_S)} - \|\boldsymbol{\xi}^{n+\theta} - \boldsymbol{\xi}^{n+1}\|^2_{L^2(\Omega_S)}\\ &\qquad = (2\theta-1)\left\|\boldsymbol{\xi}^{n+1} - \boldsymbol{\xi}^{n}\right\|^2_{L^2(\Omega_S)},\end{aligned} \tag{5.5}$$

noting that $(2\theta-1) \geq 0$ since $\theta \in [\frac{1}{2}, 1]$. Similarly, using (3.10a), we can write:

$$\|\boldsymbol{\eta}^{n+\theta} - \boldsymbol{\eta}^{n}\|^2_S - \|\boldsymbol{\eta}^{n+\theta} - \boldsymbol{\eta}^{n+1}\|^2_S = (2\theta-1)\left\|\boldsymbol{\eta}^{n+1} - \boldsymbol{\eta}^{n}\right\|^2_S. \tag{5.6}$$

Using (5.5) and (5.6), the solid estimate (5.4) becomes:

$$\begin{aligned}0 = &\frac{\rho_S}{2\tau}\left(\|\boldsymbol{\xi}^{n+1}\|^2_{L^2(\Omega_S)} - \|\boldsymbol{\xi}^{n}\|^2_{L^2(\Omega_S)}\right) + \frac{\rho_S(2\theta-1)}{2\tau}\left\|\boldsymbol{\xi}^{n+1} - \boldsymbol{\xi}^{n}\right\|^2_{L^2(\Omega_S)}\\ &+ \frac{1}{2\tau}\left(\|\boldsymbol{\eta}^{n+1}\|^2_S - \|\boldsymbol{\eta}^{n}\|^2_S\right) + \frac{(2\theta-1)}{2\tau}\left\|\boldsymbol{\eta}^{n+1} - \boldsymbol{\eta}^{n}\right\|^2_S\\ &+ \int_\Gamma \boldsymbol{\sigma}_F(\boldsymbol{u}^{n+\theta}, p^{n+\theta})\boldsymbol{n}_F \cdot \boldsymbol{\xi}^{n+\theta}.\end{aligned} \tag{5.7}$$

In a similar way, to derive an estimate for the fluid part we multiply (3.9a) by $\theta\boldsymbol{u}^{n+\theta}$, (3.9b) by $p^{n+\theta}$, and (3.13) by $(1-\theta)\boldsymbol{u}^{n+\theta}$, add together and integrate over $\Omega_F$, which results in:

$$\begin{aligned}&\frac{\rho_F}{2\tau}\left(\|\boldsymbol{u}^{n+1}\|^2_{L^2(\Omega_F)} - \|\boldsymbol{u}^{n}\|^2_{L^2(\Omega_F)} + \|\boldsymbol{u}^{n+\theta} - \boldsymbol{u}^{n}\|^2_{L^2(\Omega_F)}\right)\\ &\quad - \frac{\rho_F}{2\tau}\|\boldsymbol{u}^{n+\theta} - \boldsymbol{u}^{n+1}\|^2_{L^2(\Omega_F)} + 2\mu_F\|\boldsymbol{D}(\boldsymbol{u}^{n+\theta})\|^2_{L^2(\Omega_F)}\\ &= \int_\Gamma \boldsymbol{\sigma}_F(\boldsymbol{u}^{n+\theta}, p^{n+\theta})\boldsymbol{n}_F \cdot \boldsymbol{u}^{n+\theta} + \int_{\Omega_F} \boldsymbol{f}_F(t^{n+\theta}) \cdot \boldsymbol{u}^{n+\theta}\\ &\quad + \int_{\Gamma_F^{in}} p_{in}(t^{n+\theta})\boldsymbol{u}^{n+\theta} \cdot \boldsymbol{n}_F + \int_{\Gamma_F^{out}} p_{out}(t^{n+\theta})\boldsymbol{u}^{n+\theta} \cdot \boldsymbol{n}_F.\end{aligned}$$

Note that using (3.11), we have:

$$\|\boldsymbol{u}^{n+\theta} - \boldsymbol{u}^{n}\|^2_{L^2(\Omega_F)} - \|\boldsymbol{u}^{n+\theta} - \boldsymbol{u}^{n+1}\|^2_{L^2(\Omega_F)} = (2\theta-1)\|\boldsymbol{u}^{n+1} - \boldsymbol{u}^{n}\|^2_{L^2(\Omega_F)}.$$

Hence, the estimate for the fluid problem reads as follows:

$$\begin{aligned}&\frac{\rho_F}{2\tau}\left(\|\boldsymbol{u}^{n+1}\|^2_{L^2(\Omega_F)} - \|\boldsymbol{u}^{n}\|^2_{L^2(\Omega_F)}\right) + \frac{\rho_F(2\theta-1)}{2\tau}\|\boldsymbol{u}^{n+1} - \boldsymbol{u}^{n}\|^2_{L^2(\Omega_F)}\\ &\quad + 2\mu_F\|\boldsymbol{D}(\boldsymbol{u}^{n+\theta})\|^2_{L^2(\Omega_F)} = \int_\Gamma \boldsymbol{\sigma}_F(\boldsymbol{u}^{n+\theta}, p^{n+\theta})\boldsymbol{n}_F \cdot \boldsymbol{u}^{n+\theta}\end{aligned}$$

$$+\int_{\Omega_F} \boldsymbol{f}_F(t^{n+\theta})\cdot\boldsymbol{u}^{n+\theta}+\int_{\Gamma_F^{in}} p_{in}(t^{n+\theta})\boldsymbol{u}^{n+\theta}\cdot\boldsymbol{n}_F$$
$$+\int_{\Gamma_F^{out}} p_{out}(t^{n+\theta})\boldsymbol{u}^{n+\theta}\cdot\boldsymbol{n}_F. \tag{5.8}$$

Combining solid (5.7) and fluid (5.8) estimates and using (3.9c), we obtain:

$$\begin{aligned}
&\frac{\rho_S}{2\tau}\left(\|\boldsymbol{\xi}^{n+1}\|^2_{L^2(\Omega_S)}-\|\boldsymbol{\xi}^{n}\|^2_{L^2(\Omega_S)}\right)+\frac{\rho_S(2\theta-1)}{2\tau}\left\|\boldsymbol{\xi}^{n+1}-\boldsymbol{\xi}^{n}\right\|^2_{L^2(\Omega_S)}\\
&\quad+\frac{1}{2\tau}\left(\|\boldsymbol{\eta}^{n+1}\|^2_{S}-\|\boldsymbol{\eta}^{n}\|^2_{S}\right)+\frac{(2\theta-1)}{2\tau}\left\|\boldsymbol{\eta}^{n+1}-\boldsymbol{\eta}^{n}\right\|^2_{S}+\frac{\rho_F}{2\tau}\|\boldsymbol{u}^{n+1}\|^2_{L^2(\Omega_F)}\\
&\quad-\frac{\rho_F}{2\tau}\|\boldsymbol{u}^{n}\|^2_{L^2(\Omega_F)}+\frac{\rho_F(2\theta-1)}{2\tau}\|\boldsymbol{u}^{n+1}-\boldsymbol{u}^{n}\|^2_{L^2(\Omega_F)}+2\mu_F\|\boldsymbol{D}(\boldsymbol{u}^{n+\theta})\|^2_{L^2(\Omega_F)}\\
&=\int_{\Omega_F} \boldsymbol{f}_F(t^{n+\theta})\cdot\boldsymbol{u}^{n+\theta}+\int_{\Gamma_F^{in}} p_{in}(t^{n+\theta})\boldsymbol{u}^{n+\theta}\cdot\boldsymbol{n}_F\\
&\quad+\int_{\Gamma_F^{out}} p_{out}(t^{n+\theta})\boldsymbol{u}^{n+\theta}\cdot\boldsymbol{n}_F.
\end{aligned}\tag{5.9}$$

Using the Cauchy–Schwarz, Trace, Poincaré and Korn inequalities [11], we can estimate:

$$\begin{aligned}
&\int_{\Omega_F} \boldsymbol{f}_F(t^{n+\theta})\cdot\boldsymbol{u}^{n+\theta}+\int_{\Gamma_F^{in}} p_{in}(t^{n+\theta})\boldsymbol{u}^{n+\theta}\cdot\boldsymbol{n}_F+\int_{\Gamma_F^{out}} p_{out}(t^{n+\theta})\boldsymbol{u}^{n+\theta}\cdot\boldsymbol{n}_F\\
&\le\frac{C_1}{\mu_F}\|\boldsymbol{f}_F(t^{n+\theta})\|^2_{L^2(\Omega_F)}+\frac{C_2}{\mu_F}\|p_{in}(t^{n+\theta})\|^2_{L^2(\Gamma_F^{in})}+\frac{C_2}{\mu_F}\|p_{out}(t^{n+\theta})\|^2_{L^2(\Gamma_F^{out})}\\
&\quad+\mu_F\|\boldsymbol{D}(\boldsymbol{u}^{n+\theta})\|^2_{L^2(\Omega_F)},
\end{aligned}\tag{5.10}$$

where $C_1$ and $C_2$ do not depend on the time-discretization parameter $\tau$. Combining (5.10) with (5.9), summing from $n=2$ to $N-1$ and multiplying by $\tau$ yields the desired estimate. □

## 6. Extension to Moving Domain Fluid–Structure Interaction

In this section, we extend the model and numerical scheme presented in Algorithm 1 to describe a moving domain FSI problem. We assume that the structure equations are given in the Lagrangian framework, with respect to a reference domain $\hat{\Omega}_S$. The fluid and structure domains at time $t$ will be denoted as $\Omega_F(t)$ and $\Omega_S(t)$, respectively. The fluid equations will be described in the ALE formulation.

To track the deformation of the fluid domain in time, we introduce a smooth, invertible, ALE mapping $\mathcal{A}:\hat{\Omega}_F\times[0,T]\to\Omega_F(t)$ given by

$$\mathcal{A}(\boldsymbol{X},t)=\boldsymbol{X}+\boldsymbol{\eta}_F(\boldsymbol{X},t),\qquad \text{for all } \boldsymbol{X}\in\hat{\Omega}_F, t\in[0,T],$$

where $\boldsymbol{\eta}_F$ denotes the displacement of the fluid domain. The fluid domain is determined by $\Omega_F(t)=\mathcal{A}(\hat{\Omega}_F,t)$. We denote the fluid deformation gradient by $\boldsymbol{F}=\nabla\mathcal{A}$ and its determinant by $J$. We assume that $\boldsymbol{\eta}_F$ equals the structure displacement on $\hat{\Gamma}$, and is arbitrarily extended into the fluid domain $\hat{\Omega}_F$ [39]. To simplify the notation, we will write

$$\int_{\Omega(t^m)}\boldsymbol{v}^n \quad\text{instead of}\quad \int_{\Omega(t^m)}\boldsymbol{v}^n\circ\mathcal{A}(t^n)\circ\mathcal{A}^{-1}(t^m)$$

whenever we need to integrate $\boldsymbol{v}^n$ on a domain $\Omega(t^m)$, for $m\neq n$.

To model the fluid flow, we consider the Navier–Stokes equations in the ALE form [8,9,39], given by

$$\begin{aligned}
&\rho_F\left(\partial_t\boldsymbol{u}|_{\hat{\Omega}_F}+(\boldsymbol{u}-\boldsymbol{w})\cdot\nabla\boldsymbol{u}\right)=\nabla\cdot\boldsymbol{\sigma}_F(\boldsymbol{u},p)+\boldsymbol{f}_F && \text{in } \Omega_F(t)\times(0,T),\\
&\nabla\cdot\boldsymbol{u}=0 && \text{in } \Omega_F(t)\times(0,T),
\end{aligned}$$

where $\boldsymbol{w} = \partial_t \boldsymbol{x}|_{\hat{\Omega}_F} = \partial_t \mathcal{A} \circ \mathcal{A}^{-1}$ is the domain velocity. We note that $\partial_t \boldsymbol{u}|_{\hat{\Omega}_F}$ denotes the Eulerian description of the ALE field $\partial_t \boldsymbol{u} \circ \mathcal{A}$ [29], *i.*e.,

$$\partial_t \boldsymbol{u}(\boldsymbol{x}, t)|_{\hat{\Omega}_F} = \partial_t \boldsymbol{u}(\mathcal{A}^{-1}(\boldsymbol{x}, t), t).$$

The structure model remains the same as in (2.3). Hence, the fully-coupled, moving domain FSI problem is given by

$$\begin{aligned}
&\rho_F \left( \partial_t \boldsymbol{u}|_{\hat{\Omega}_F} + (\boldsymbol{u} - \boldsymbol{w}) \cdot \nabla \boldsymbol{u} \right) = \nabla \cdot \boldsymbol{\sigma}_F(\boldsymbol{u}, p) \\
&\quad + \boldsymbol{f}_F && \text{in } \Omega_F(t) \times (0,T), && (6.1a)\\
&\nabla \cdot \boldsymbol{u} = 0 && \text{in } \Omega_F(t) \times (0,T), && (6.1b)\\
&\partial_t \boldsymbol{\eta} = \boldsymbol{\xi} && \text{in } \hat{\Omega}_S \times (0,T), && (6.1c)\\
&\rho_S \partial_t \boldsymbol{\xi} = \nabla \cdot \boldsymbol{\sigma}_S(\boldsymbol{\eta}) && \text{in } \hat{\Omega}_S \times (0,T), && (6.1d)\\
&\boldsymbol{u} \circ \mathcal{A} = \boldsymbol{\xi} && \text{on } \hat{\Gamma} \times (0,T), && (6.1e)\\
&J \boldsymbol{\sigma}_F \boldsymbol{F}^{-T} \boldsymbol{n}_F + \boldsymbol{\sigma}_S \boldsymbol{n}_S = 0 && \text{on } \hat{\Gamma} \times (0,T), && (6.1f)
\end{aligned}$$

complemented with boundary conditions (2.2), (2.5) and (2.6), and initial conditions (2.9).

To solve problem (6.1), we extend the approach presented in Algorithm 1. In the following, we denote

$$\widehat{\boldsymbol{\sigma}_F \boldsymbol{n}_F}_{(\kappa)}^{n+\theta} = J_{(\kappa)}^{n+\theta} \boldsymbol{\sigma}_F(\boldsymbol{u}_{(\kappa)}^{n+\theta}, p_{(\kappa)}^{n+\theta})(\boldsymbol{F}_{\kappa}^{n+\theta})^{-T} \boldsymbol{n}_{F,(\kappa)}^{n+\theta}.$$

The resulting scheme is presented as follows.

**Algorithm 2.** *Given $\boldsymbol{u}^0$ in $\hat{\Omega}_F$, and $\boldsymbol{\eta}^0, \boldsymbol{\xi}^0$ in $\hat{\Omega}_S$, we first need to compute $p^\theta, p^{1+\theta}, \boldsymbol{u}^1, \boldsymbol{u}^2, \boldsymbol{\eta}_F^1, \boldsymbol{w}^1$ and $\boldsymbol{\eta}^1, \boldsymbol{\eta}^2, \boldsymbol{\xi}^1, \boldsymbol{\xi}^2$ with a second-order method. A monolithic method could be used. Then, for all $n \geq 2$, compute the following steps:*

Step 1. *Set the initial guesses as the linearly extrapolated values:*

$$\boldsymbol{\eta}_{(0)}^{n+\theta} = \Big(1 + \theta\Big)\boldsymbol{\eta}^n - \theta \boldsymbol{\eta}^{n-1},$$

*and similarly for $\boldsymbol{\xi}_{(0)}^{n+\theta}, \boldsymbol{u}_{(0)}^{n+\theta}$. The pressure initial guess is defined as*

$$p_{(0)}^{n+\theta} = (1+\tau) p^{n-1+\theta} - \tau p^{n-2+\theta}.$$

*For $\kappa \geq 0$, compute until convergence the* **Backward Euler** *partitioned problem:*

$$\text{Solid:} \begin{cases}
\frac{\boldsymbol{\eta}_{(\kappa+1)}^{n+\theta} - \boldsymbol{\eta}^n}{\theta\tau} = \boldsymbol{\xi}_{(\kappa+1)}^{n+\theta} & \text{in } \hat{\Omega}_S, \\
\rho_S \frac{\boldsymbol{\xi}_{(\kappa+1)}^{n+\theta} - \boldsymbol{\xi}^n}{\theta\tau} = \nabla \cdot \boldsymbol{\sigma}_S(\boldsymbol{\eta}_{(\kappa+1)}^{n+\theta}) & \text{in } \hat{\Omega}_S, \\
\alpha \boldsymbol{\xi}_{(\kappa+1)}^{n+\theta} + \boldsymbol{\sigma}_S(\boldsymbol{\eta}_{(\kappa+1)}^{n+\theta}) \boldsymbol{n}_S = \alpha \boldsymbol{u}_{(\kappa)}^{n+\theta} & \\
\quad - \widehat{\boldsymbol{\sigma}_F \boldsymbol{n}_F}_{(\kappa)}^{n+\theta} & \text{on } \hat{\Gamma},
\end{cases}$$

$$\text{Geo.:} \begin{cases}
-\Delta \boldsymbol{\eta}_{F,(\kappa+1)}^{n+\theta} = 0 & \text{in } \hat{\Omega}_F, \\
\boldsymbol{\eta}_{F,(\kappa+1)}^{n+\theta} = 0 & \text{on } \hat{\Gamma}_F^{in} \cup \hat{\Gamma}_F^{out}, \\
\boldsymbol{\eta}_{F,(\kappa+1)}^{n+\theta} = \boldsymbol{\eta}_{(\kappa+1)}^{n+\theta} & \text{on } \hat{\Gamma}, \\
\boldsymbol{w}_{(\kappa+1)}^{n+\theta} = \frac{\boldsymbol{\eta}_{F,(\kappa+1)}^{n+\theta} - \boldsymbol{\eta}_F^n}{\theta\tau} & \text{in } \hat{\Omega}_F, \\
\Omega_{F,(\kappa+1)}^{n+\theta} = (\mathbf{I} + \boldsymbol{\eta}_{F,(\kappa+1)}^{n+\theta}) \hat{\Omega}_F, &
\end{cases}$$

$$\text{Fluid:}\begin{cases}\rho_F \frac{\boldsymbol{u}_{(\kappa+1)}^{n+\theta}-\boldsymbol{u}^n}{\theta\tau} & \\ \quad +\rho_F\left(\boldsymbol{u}_{(\kappa)}^{n+\theta}-\boldsymbol{w}_{(\kappa+1)}^{n+\theta}\right)\cdot\nabla\boldsymbol{u}_{(\kappa+1)}^{n+\theta} & \\ \quad =\nabla\cdot\boldsymbol{\sigma}_F(\boldsymbol{u}_{(\kappa+1)}^{n+\theta},p_{(\kappa+1)}^{n+\theta})+\boldsymbol{f}_F(t^{n+\theta}) & \text{in } \Omega_{F,(\kappa+1)}^{n+\theta},\\ \nabla\cdot\boldsymbol{u}_{(\kappa+1)}^{n+\theta}=0 & \text{in } \Omega_{F,(\kappa+1)}^{n+\theta},\\ \alpha\boldsymbol{u}_{(\kappa+1)}^{n+\theta}-\boldsymbol{\sigma}_F(\boldsymbol{u}_{(\kappa)}^{n+\theta},p_{(\kappa)}^{n+\theta})\boldsymbol{n}_{F,(\kappa)}^{n+\theta} & \\ \quad =\alpha\boldsymbol{\xi}_{(\kappa+1)}^{n+\theta}-\boldsymbol{\sigma}_F(\boldsymbol{u}_{(\kappa+1)}^{n+\theta},p_{(\kappa+1)}^{n+\theta})\boldsymbol{n}_{F,(\kappa+1)}^{n+\theta} & \text{on } \Gamma_{(\kappa+1)}^{n+\theta}.\end{cases}$$

*The converged solutions,*

$$\boldsymbol{\eta}_{(\kappa)}^{n+\theta},\boldsymbol{\xi}_{(\kappa)}^{n+\theta},\boldsymbol{u}_{(\kappa)}^{n+\theta},p_{(\kappa)}^{n+\theta},\boldsymbol{w}_{(\kappa)}^{n+\theta},\boldsymbol{\eta}_{F,(\kappa)}^{n+\theta}\xrightarrow{\kappa\to\infty}\boldsymbol{\eta}^{n+\theta},\boldsymbol{\xi}^{n+\theta},\boldsymbol{u}^{n+\theta},p^{n+\theta},\boldsymbol{w}^{n+\theta},\boldsymbol{\eta}_F^{n+\theta},$$

*then satisfy:*

$$\text{Solid:}\begin{cases}\frac{\boldsymbol{\eta}^{n+\theta}-\boldsymbol{\eta}^n}{\theta\tau}=\boldsymbol{\xi}^{n+\theta} & \text{in } \hat{\Omega}_S,\\ \rho_S\frac{\boldsymbol{\xi}^{n+\theta}-\boldsymbol{\xi}^n}{\theta\tau}=\nabla\cdot\boldsymbol{\sigma}_S(\boldsymbol{\eta}^{n+\theta}) & \text{in } \hat{\Omega}_S,\\ \boldsymbol{\sigma}_S(\boldsymbol{\eta}^{n+\theta})\boldsymbol{n}_S=-\widehat{\boldsymbol{\sigma}_F\boldsymbol{n}_F}^{n+\theta} & \text{on } \hat{\Gamma},\end{cases}$$

$$\text{Geo.:}\begin{cases}-\Delta\boldsymbol{\eta}_F^{n+\theta}=0 & \text{in } \hat{\Omega}_F,\\ \boldsymbol{\eta}_F^{n+\theta}=0 & \text{on } \hat{\Gamma}_F^{in}\cup\hat{\Gamma}_F^{out},\\ \boldsymbol{\eta}_F^{n+\theta}=\boldsymbol{\eta}^{n+\theta} & \text{on } \hat{\Gamma},\\ \boldsymbol{w}^{n+\theta}=\frac{\boldsymbol{\eta}_F^{n+\theta}-\boldsymbol{\eta}_F^n}{\theta\tau} & \text{in } \hat{\Omega}_F,\\ \Omega_F^{n+\theta}=(\mathbf{I}+\boldsymbol{\eta}_F^{n+\theta})\hat{\Omega}_F, & \end{cases}$$

$$\text{Fluid:}\begin{cases}\rho_F\frac{\boldsymbol{u}^{n+\theta}-\boldsymbol{u}^n}{\theta\tau}+\left(\boldsymbol{u}^{n+\theta}-\boldsymbol{w}^{n+\theta}\right)\cdot\nabla\boldsymbol{u}^{n+\theta} & \\ \quad =\nabla\cdot\boldsymbol{\sigma}_F(\boldsymbol{u}^{n+\theta},p^{n+\theta})+\boldsymbol{f}_F(t^{n+\theta}) & \text{in } \Omega_F^{n+\theta},\\ \nabla\cdot\boldsymbol{u}^{n+\theta}=0 & \text{in } \Omega_F^{n+\theta},\\ \boldsymbol{u}^{n+\theta}=\boldsymbol{\xi}^{n+\theta} & \text{on } \Gamma^{n+\theta}.\end{cases}$$

Step 2. *Now evaluate the following:*

$$\text{Solid:}\begin{cases}\boldsymbol{\eta}^{n+1}=\frac{1}{\theta}\boldsymbol{\eta}^{n+\theta}-\frac{1-\theta}{\theta}\boldsymbol{\eta}^n & \textit{in } \hat{\Omega}_S,\\ \boldsymbol{\xi}^{n+1}=\frac{1}{\theta}\boldsymbol{\xi}^{n+\theta}-\frac{1-\theta}{\theta}\boldsymbol{\xi}^n & \textit{in } \hat{\Omega}_S,\end{cases}$$

$$\text{Geo.:}\begin{cases}-\Delta\boldsymbol{\eta}_F^{n+1}=0 & \textit{in } \hat{\Omega}_F,\\ \boldsymbol{\eta}_F^{n+1}=0 & \text{on } \hat{\Gamma}_F^{in}\cup\hat{\Gamma}_F^{out},\\ \boldsymbol{\eta}_F^{n+1}=\boldsymbol{\eta}^{n+1} & \textit{on } \hat{\Gamma},\\ \boldsymbol{w}^{n+1}=\frac{\boldsymbol{\eta}_F^{n+1}-\boldsymbol{\eta}_F^{n+\theta}}{(1-\theta)\tau} & \textit{in } \hat{\Omega}_F,\\ \Omega_F^{n+1}=(\mathbf{I}+\boldsymbol{\eta}_F^{n+1})\hat{\Omega}_F, & \end{cases}$$

$$\text{Fluid:}\begin{cases}\boldsymbol{u}^{n+1}=\frac{1}{\theta}\boldsymbol{u}^{n+\theta}-\frac{1-\theta}{\theta}\boldsymbol{u}^n & \textit{in } \Omega_F^{n+1}.\end{cases}$$

Set $n=n+1$, and go back to Step 1.

The problems above are complimented with the same boundary conditions as in Algorithm 1.

## 7. Numerical Examples

In this section, we investigate the accuracy and the rates of convergence of the proposed method. To discretize the problem in space, we use the finite element method with uniform, conforming meshes, and denote the mesh size by $h$. The numerical method is implemented in the finite element solver FreeFem++ [36]. The benchmark problem presented in Example 1 is based on the method of manufactured solutions. In this example, we compute the convergence rates obtained with Algorithm 1 for different values of parameters $\theta, \alpha$ and the tolerance $\epsilon$. In the second example, we consider a moving domain benchmark problem commonly used to test FSI solvers. Using this example, we compare the results obtained using Algorithm 2 to a loosely-coupled partitioned scheme [46].

### 7.1. Example 1

In this example we use a method of manufactured solutions to investigate the accuracy of the computational method presented in Algorithm 1. For this purpose, the set of problems we are solving is based on the time-dependent Stokes equations and elastodynamics equations with added forcing terms:

$$\begin{aligned} \rho_F \partial_t \boldsymbol{u} &= \nabla \cdot \boldsymbol{\sigma}_F(\boldsymbol{u}, p) + \boldsymbol{f}_F && \text{in } \Omega_F \times (0,T), \\ \nabla \cdot \boldsymbol{u} &= g && \text{in } \Omega_F \times (0,T), \\ \rho_S \partial_t \boldsymbol{\xi} &= \nabla \cdot \boldsymbol{\sigma}_S(\boldsymbol{\eta}) + \boldsymbol{f}_S && \text{in } \Omega_S \times (0,T). \end{aligned}$$

The FSI problem is defined in a unit square domain such that the fluid domain resides in the lower half, $\Omega_F = (0,1) \times (0,0.5)$, and the solid domain occupies the upper half, $\Omega_S = (0,1) \times (0.5,1)$. We assume that the FSI problem is linear and that the domain remains fixed. We use the following physical parameters: $\lambda_S = \mu_S = \rho_S = \rho_F = \mu_F = 1$. The exact solutions are given by:

$$\begin{aligned} \boldsymbol{\eta}_{ref} &= \begin{bmatrix} 10^{-3} 2x(1-x)y(1-y)e^t \\ 10^{-3} x(1-x)y(1-y)e^t \end{bmatrix}, \\ \boldsymbol{u}_{ref} &= \begin{bmatrix} 10^{-3} 2x(1-x)y(1-y)e^t \\ 10^{-3} x(1-x)y(1-y)e^t \end{bmatrix}, \\ p_{ref} &= -10^{-3} e^t \lambda_S \left(2(1-2x)y(1-y) + x(1-x)(1-2y)\right). \end{aligned}$$

Using the exact solutions, we compute the forcing terms $\boldsymbol{f}_F, g$ and $\boldsymbol{f}_S$. We impose Dirichlet boundary conditions on the bottom of the fluid domain, and Neumann conditions on other external boundaries. The sub-iterative portion of the scheme, defined by equations (3.6)–(3.7), is run until the relative errors between two consecutive approximations for the fluid velocity, structure velocity and displacement are less than a given tolerance, $\epsilon$. To discretize the problem in space, we used $\mathbb{P}_2$ elements for the fluid velocity and solid displacement and velocity, and $\mathbb{P}_1$ elements for the pressure. In order to compute the rates of convergence, we first define the errors for the solid displacement and velocity, and fluid velocity as:

$$e_{\boldsymbol{\eta}} = \frac{\|\boldsymbol{\eta} - \boldsymbol{\eta}_{ref}\|_S^2}{\|\boldsymbol{\eta}_{ref}\|_S^2}, \quad e_{\boldsymbol{\xi}} = \frac{\|\boldsymbol{\xi} - \boldsymbol{\xi}_{ref}\|_{L^2(\Omega_S)}}{\|\boldsymbol{\xi}_{ref}\|_{L^2(\Omega_S)}}, \quad e_F = \frac{\|\boldsymbol{u} - \boldsymbol{u}_{ref}\|_{L^2(\Omega_F)}}{\|\boldsymbol{u}_{ref}\|_{L^2(\Omega_F)}},$$

respectively.

Recall that the Robin-type boundary conditions at the interface include a combination parameter, $\alpha$, which places an emphasis on the coupling condition of choice (i.e. kinematic or dynamic). In particular, case $\alpha = 0$ gives the dynamic coupling condition, while $\alpha = \infty$ leads to the kinematic coupling condition. As similar Robin boundary conditions have been used by other authors, finding an optimal value of $\alpha$ has been previously investigated. In particular, a heuristic formula for $\alpha$ is given by [31]:

$$\alpha_{opt} = \frac{\rho_S H_S}{\tau} + \beta H_S \tau, \tag{7.1}$$

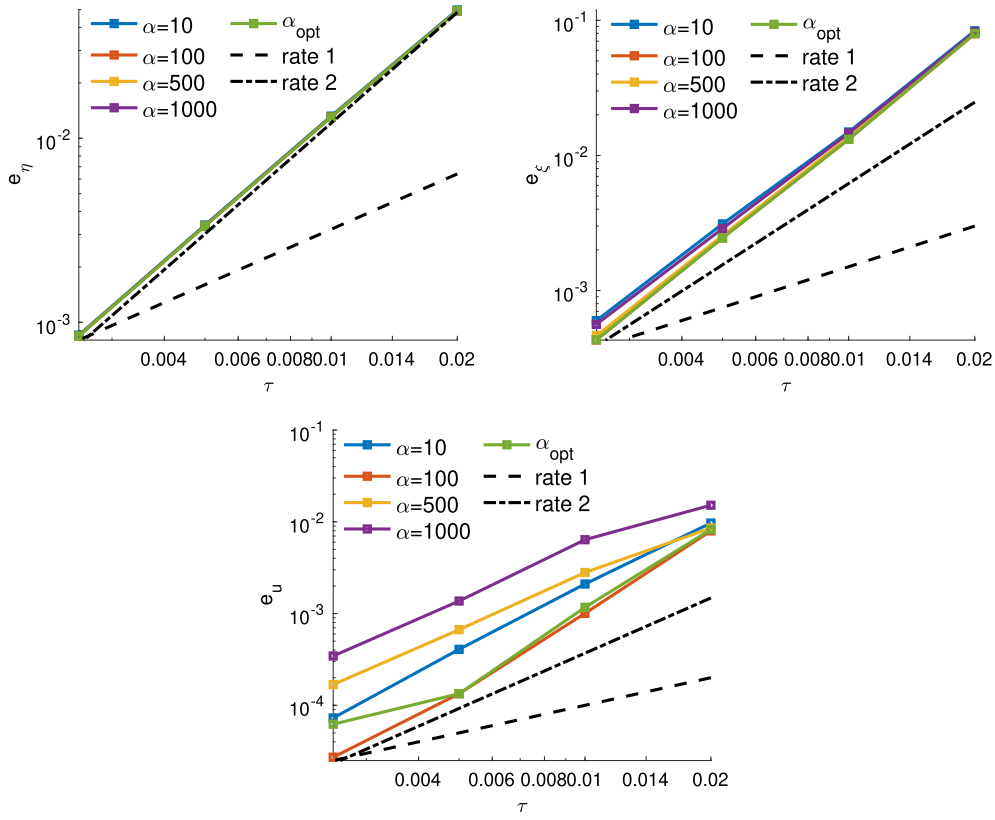


FIG. 2. Example 1: Errors obtained with $\theta = 0.5$ and $\epsilon = 10^{-4}$ by varying $\alpha$ for the solid displacement, $\boldsymbol{\eta}$, (top-left), solid velocity, $\boldsymbol{\xi}$, (top-right), and fluid velocity, $\boldsymbol{u}$, (bottom) at the final time

where $H_S$ is the height of the solid domain and $\beta = \dfrac{E}{1-\nu^2}(4\rho_1^2 - 2(1-\nu)\rho_2^2)$, with $E$ denoting the Young's modulus, $\nu$ representing the Poisson's ratio and $\rho_1$ and $\rho_2$ signifying the mean and Gaussian curvatures of the fluid–structure interface, respectively. In our case, we compute $\beta$ as:

$$\beta = \frac{E}{(1-\nu^2)R^2},$$

where $R$ is the height of the fluid domain. In addition to $\alpha_{opt}$, we explore other values: $\alpha = 10, 100, 500$ and 1000.

In the first test, we set $\epsilon = 10^{-4}$ and $\theta = \frac{1}{2}$. We recall that we expect to obtain the convergence rate of $\mathcal{O}(\tau^2)$ because for $\theta = \frac{1}{2}$, the discretization method corresponds to the midpoint rule. To compute the rates of convergence, we use the following time and space discretization parameters:

$$\{\tau, h\} = \left\{\frac{0.02}{2^i}, \frac{0.25}{2^i}\right\}_{i=0}^{3}.$$

The final time is $T = 0.3$ s. The rates of convergence obtained for different values of $\alpha$ are shown in Fig. 2.

Overall, Fig. 2 shows very promising convergence rates, averaging around 2 or above for all variables. The errors for $\boldsymbol{\eta}$ are almost indistinguishable for different values of $\alpha$, showing a near-perfect convergence rate of 2. For $\boldsymbol{\xi}$, we observe that there is only a very slight disadvantage for $\alpha = 10$ and 1000, with errors only slightly increased at the finest mesh size and time step; the convergence rates for all values of $\alpha$

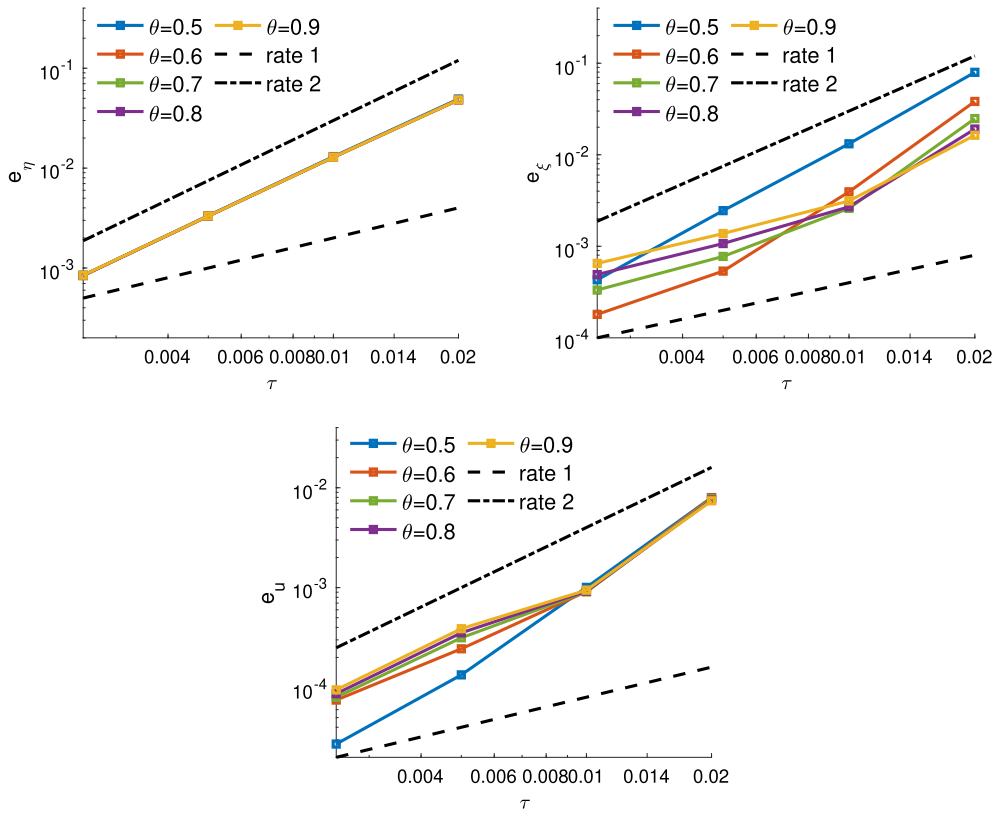


FIG. 3. Example 1: Errors obtained with $\alpha = 100$ and $\epsilon = 10^{-4}$ by varying $\theta$ for the solid displacement, $\boldsymbol{\eta}$, (top-left), solid velocity, $\boldsymbol{\xi}$, (top-right), and fluid velocity, $\boldsymbol{u}$, (bottom) at the final time

are mostly better than 2. Finally, for $\boldsymbol{u}$, the convergence rates slightly exceed 2 for the most part with smallest errors when $\alpha = 100$ and $\alpha_{opt}$.

In the next simulation, we investigate the effect of $\theta$ on the convergence rates. In particular, we use $\theta = 0.5, 0.6, 0.7, 0.8$ and 0.9, keeping the same values of $\epsilon, \tau$ and $h$, and using $\alpha = 100$. The rates of convergence are shown in Fig. 3. As before, the errors for $\boldsymbol{\eta}$ show a convergence rate of 2 for all values of $\theta$. For $\boldsymbol{\xi}$, we observe that $\theta$=0.5 maintains a convergence rate of 2 or greater, while rates for other values of $\theta$ are larger than 2 for the coarsest mesh and time step and decrease to values close to 1 at the most-refined time step and mesh size. We note that $\theta$=0.5 has larger errors than either $\theta = 0.6$ or 0.7, albeit on the order of magnitude of $10^{-4}$. Finally, for $\boldsymbol{u}$, the convergence rates are at least 2 for larger values of time step and mesh size, but similar as in the previous case, they drop down to $\mathcal{O}(\tau)$ as $\theta$ increases. The errors are the smallest when $\theta = 0.5$.

In the next test, we continue to evaluate similar conditions as in Fig. 2, but this time we use a tolerance of $\epsilon = 10^{-3}$ instead of $10^{-4}$. As in Fig. 2, we use $\theta = \frac{1}{2}$ in conjunction with a range of different values of $\alpha$. Figure 4 shows the errors for the structure displacement (top-left), structure velocity (top-right), and fluid velocity (bottom).

In this case, the rates for the solid velocity and displacement remain close to 2, while the rates for the fluid velocity become sub-optimal in most cases.

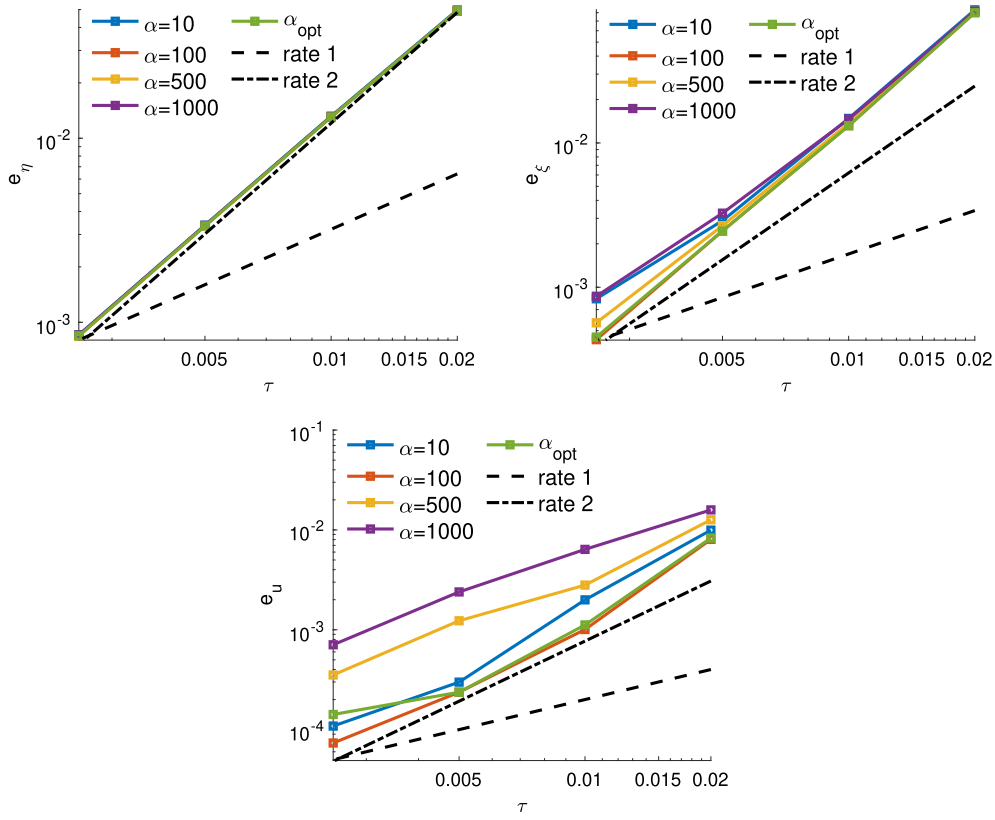


FIG. 4. Example 1: Errors obtained with $\theta = 0.5$ and $\epsilon = 10^{-3}$ by varying $\alpha$ for the solid displacement, $\boldsymbol{\eta}$, (top-left), solid velocity, $\boldsymbol{\xi}$, (top-right), and fluid velocity, $\boldsymbol{u}$, (bottom) at the final time

To correct the loss of accuracy that occurs for a larger value of $\epsilon$, we model the same setting as in Fig. 4, but halve $\epsilon$ at the same rate as $\tau$, i.e., using the following set of parameters:

$$\{\tau, h, \epsilon\} = \left\{ \frac{0.02}{2^i}, \frac{0.25}{2^i}, \frac{10^{-3}}{2^i} \right\}_{i=0}^{3}.$$

Figure 5 shows the rates of convergence obtained in this case. We observe that the convergence rates for fluid and solid velocity improve when $\epsilon$ is reduced at the same rate as $\tau$.

To further emphasize the differences in the solution for different values of $\epsilon$, shown in Figs. 2, 4 and 5, the convergence rates for the fluid and solid velocity obtained using $\epsilon = 10^{-4}$, $\epsilon = 10^{-3}$, and by decreasing $\epsilon$ at the same rate as $\tau$ are shown in Table 1.

In the cases presented above, we calculated the average number of sub-iterations in the sub-iterative step of our scheme. Figure 6 shows the average number of sub-iterations obtained with $\theta = \frac{1}{2}$ and $\epsilon = 10^{-4}$ (top-left), $\epsilon = 10^{-3}$ (top-right), and with $\epsilon = \left\{ \frac{10^{-3}}{2^i} \right\}_{i=0}^{3}$ (bottom). About at most 6 sub-iterations are needed when $\epsilon = 10^{-4}$ for $\alpha = 100$ and 500. However, we notice that in all cases, the number of sub-iterations decreases to about 2 when the discretization parameters decrease. As expected, a larger number of sub-iterations is required for a smaller value of $\epsilon$. However, when $\epsilon$ decreases at the same rate as $\tau$, the number of sub-iterations stays roughly the same in most cases. When looking across all three scenarios, we note that $\alpha = 1000$ yields the lowest number of sub-iterations and $\alpha = 10$ typically results in the highest number of sub-iterations with the exception of the coarsest $\tau$ when the tolerance is fixed at $\epsilon = 10^{-4}$.

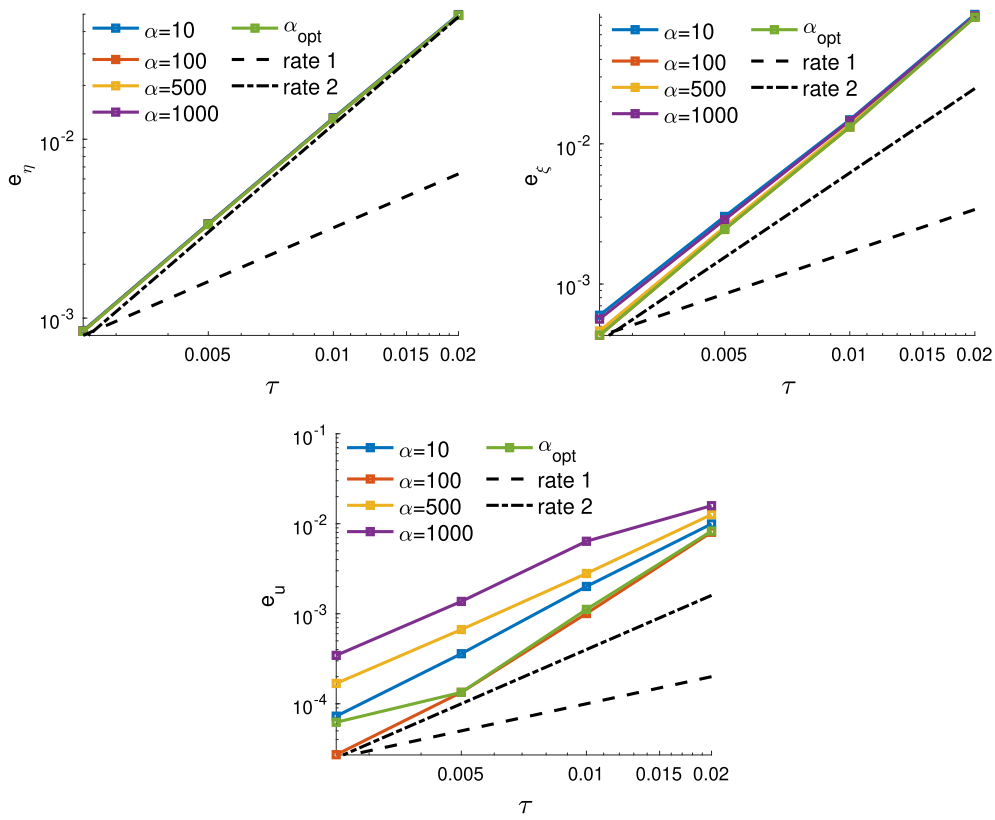


FIG. 5. Example 1: Errors, halving tolerance for each refinement, by varying $\alpha$ for the solid displacement, $\boldsymbol{\eta}$, (top-left), solid velocity, $\boldsymbol{\xi}$, (top-right), and fluid velocity, $\boldsymbol{u}$, (bottom) at the final time

TABLE 1. Example 1: Rates of convergence for the fluid and structure velocity obtained with $\theta = \frac{1}{2}$ and the following values of $\epsilon$ : $\epsilon = 10^{-4}$ (top), $\epsilon = 10^{-3}$ (middle), and $\epsilon$ decreasing at the same rate as $\tau$ (bottom)

| $\epsilon = 10^{-4}$ | $\boldsymbol{u}$ | | | | $\boldsymbol{\xi}$ | | | |
|---|---|---|---|---|---|---|---|---|
| $\alpha$ : | 10 | 100 | 500 | 1000 | 10 | 100 | 500 | 1000 |
| $\tau$ | – | – | – | – | – | – | – | – |
| $\tau/2$ | 2.21 | 2.99 | 1.61 | 1.25 | 2.49 | 2.59 | 2.56 | 2.49 |
| $\tau/4$ | 2.37 | 2.91 | 2.07 | 2.22 | 2.26 | 2.43 | 2.42 | 2.34 |
| $\tau/8$ | 2.49 | 2.30 | 2.29 | 2.29 | 2.38 | 2.51 | 2.46 | 2.35 |
| $\epsilon = 10^{-3}$ | $\boldsymbol{u}$ | | | | $\boldsymbol{\xi}$ | | | |
| $\alpha$ : | 10 | 100 | 500 | 1000 | 10 | 100 | 500 | 1000 |
| $\tau$ | – | – | – | – | – | – | – | – |
| $\tau/2$ | 2.32 | 3.00 | 2.27 | 1.31 | 2.50 | 2.60 | 2.58 | 2.49 |
| $\tau/4$ | 2.74 | 2.09 | 1.19 | 1.42 | 2.35 | 2.43 | 2.36 | 2.26 |
| $\tau/8$ | 1.46 | 1.69 | 1.80 | 2.26 | 1.80 | 2.50 | 2.24 | 2.21 |
| $\epsilon$ changing | $\boldsymbol{u}$ | | | | $\boldsymbol{\xi}$ | | | |
| $\alpha$ : | 10 | 100 | 500 | 1000 | 10 | 100 | 500 | 1000 |
| $\tau$ | – | – | – | – | – | – | – | – |
| $\tau/2$ | 2.31 | 3.00 | 2.27 | 1.31 | 2.50 | 2.60 | 2.58 | 2.49 |
| $\tau/4$ | 2.48 | 2.91 | 2.07 | 2.22 | 2.29 | 2.43 | 2.42 | 2.34 |
| $\tau/8$ | 2.31 | 2.30 | 2.29 | 2.29 | 2.34 | 2.51 | 2.46 | 2.35 |

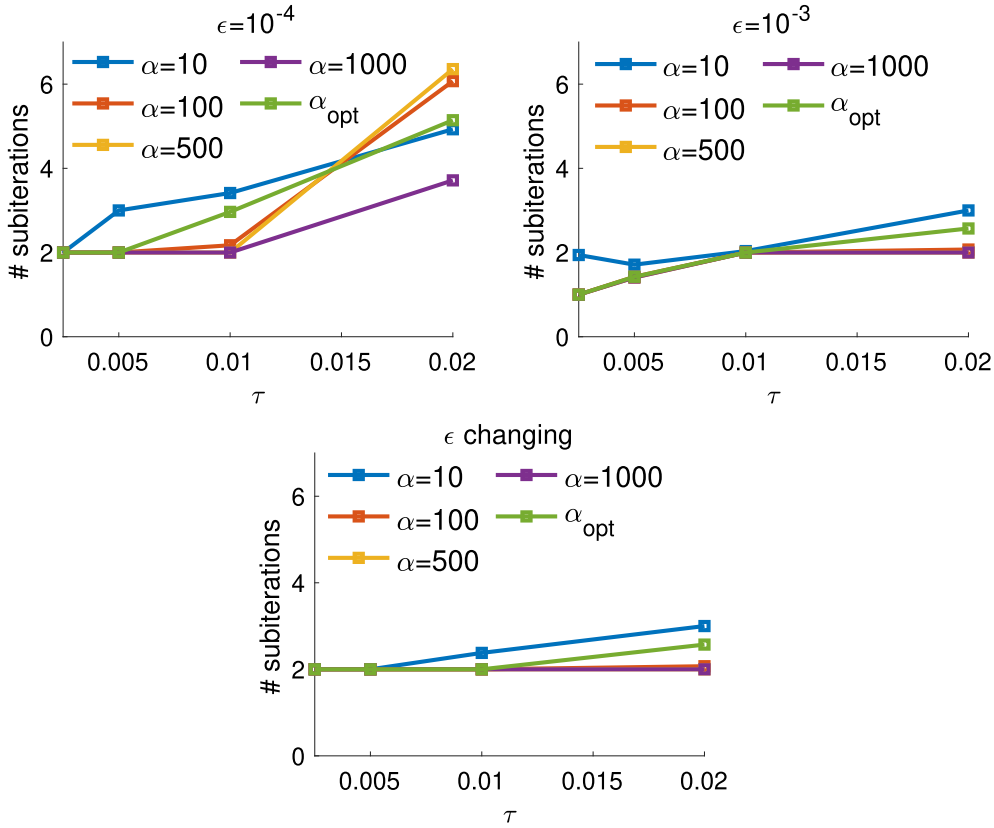


FIG. 6. Example 1: Number of sub-iterations when the tolerance is $\epsilon = 10^{-4}$ (top left), $\epsilon = 10^{-3}$ (top right), and when $\epsilon$ is halved in each run (bottom)

Finally, we compare the number of sub-iterations required by our scheme and a couple of commonly used strongly-coupled methods for FSI problems: a Robin–Neumann scheme and a Robin–Robin scheme [2]. We use $\alpha = \alpha_{opt}$ and $\theta = \frac{1}{2}$ in Algorithm 1. For the Robin–Robin method, we use

$$\alpha_f = \frac{\rho_s H_s}{\tau} + \frac{H_s E \tau}{((1-\nu^2)R^2}, \quad \alpha_s = \frac{2\rho_f}{\pi\tau},$$

where $E$ is the Young's modulus and $\nu$ is the Poisson's ratio. The same $\alpha_f$ is used for the Robin–Neumann method, with $\alpha_s = 0$. Relaxation parameter $\omega = 0.1$ is used for the Robin–Neumann method in all cases except for $\rho_S = 10$, when $\omega = 0.3$ is used. No relaxation is used for the Robin–Robin method. Table 2 shows the number of sub-iterations required by all three methods for different parameter values. In all considered cases, the proposed method features a smaller number of sub-iterations compared to other methods. We note that for Algorithm 1, the number of sub-iterations decreased as the solid density increased, and increased as the tolerance, $\epsilon$, decreased. The same behavior with respect to $\epsilon$ was observed in the Robin–Neumann and the Robin–Robin method. While the number of sub-iterations obtained using the Robin–Neumann method is quite large, we would like to point out that the same method has been previously tested on similar examples, with $\alpha_f$ computed using the same formula, without the need of any relaxation, and achieving convergence in a smaller number of iterations (e.g., 4-9 sub-iterations in [1], 4-11 sub-iterations in [31]).

TABLE 2. Example 1: The number of sub-iterations required by the Robin–Neumann (RN) method, the Robin–Robin (RR) method *[2]*, and the proposed method (Algorithm *1*) for different parameter values

| $\tau$ | $h$ | $\rho_F$ | $\rho_S$ | $\epsilon$ | RN | RR | Algorithm 1 |
|---|---|---|---|---|---|---|---|
| $10^{-2}$ | $1.25 \cdot 10^{-1}$ | 1 | 1 | $10^{-3}$ | 23 | 3.43 | 2 |
| $5 \cdot 10^{-3}$ | $1.25 \cdot 10^{-1}$ | 1 | 1 | $10^{-3}$ | 16.7 | 3.28 | 2 |
| $10^{-2}$ | $6.25 \cdot 10^{-2}$ | 1 | 1 | $10^{-3}$ | 23.06 | 3.43 | 2 |
| $10^{-2}$ | $1.25 \cdot 10^{-1}$ | 1 | 10 | $10^{-3}$ | 7.73 | 3.73 | 1.03 |
| $10^{-2}$ | $1.25 \cdot 10^{-1}$ | 10 | 1 | $10^{-3}$ | 50.56 | 3.06 | 2 |
| $10^{-2}$ | $1.25 \cdot 10^{-1}$ | 1 | 1 | $10^{-4}$ | 45.46 | 8.2 | 2.97 |

### 7.2. Example 2

In the second example, we consider a classical, moving domain benchmark problem typically used to validate FSI solvers [8] describing the fluid flow in a two-dimensional channel interacting with a deformable wall. The fluid and structure domains are defined as $\Omega_F = (0,5) \times (0,0.5)$ and $\Omega_S = (0,5) \times (0.5,0.6)$, respectively. We consider the FSI problem (6.1), where we add a linear "spring" term, $\gamma\boldsymbol{\eta}$, to the elastodynamic equation (2.3), yielding:

$$\rho_S \partial_t \boldsymbol{\xi} + \gamma\boldsymbol{\eta} = \nabla \cdot \boldsymbol{\sigma}_S(\boldsymbol{\eta}) \ \text{ in } \Omega_S \times (0,T).$$

The term $\gamma\boldsymbol{\eta}$ is obtained from the axially symmetric model and it represents a spring keeping the top and bottom boundaries in a two-dimensional model connected [8].

We use the following parameter values: $\rho_S = 1.1$ g/cm$^3$, $\mu_S = 1.67785 \cdot 10^6$ dyne/cm$^2$, $\gamma = 4 \cdot 10^6$ dyne/cm$^4$, $\lambda_S = 8.22148 \cdot 10^7$ dyne/cm$^2$, $\rho_F = 1$ g/cm$^3$, and $\mu_F = 0.035$ g/cm·s, which are within physiologically realistic values of blood flow in compliant arteries. In this example, we set $\theta = \frac{1}{2}, \epsilon = 10^{-4}$ and $\alpha = \alpha_{opt}$, given by (7.1).

The flow is driven by prescribing a time-dependent pressure drop at the inlet and outlet sections, as defined in (2.2), where

$$p_{in}(t) = \begin{cases} \dfrac{p_{max}}{2}\left[1 - \cos\left(\dfrac{2\pi t}{t_{max}}\right)\right], & \text{if } t \le t_{max} \\ 0, & \text{if } t > t_{max} \end{cases}, \quad p_{out} = 0, \tag{7.2}$$

for all $t \in (0,T)$. The pressure pulse is in effect for $t_{max} = 0.03$ s with maximum pressure $p_{max} = 1.333 \times 10^4$ dyne/cm$^2$. The final time is $T = 12$ ms, and the time step is $\tau = 10^{-4}$. At the bottom fluid boundary we prescribe symmetry conditions given by:

$$u_y = 0, \quad \frac{\partial u_x}{\partial y} = 0.$$

We assume that the structure is fixed at the edges, with zero normal stress at the external boundary, as specified in (2.5)-(2.6).

We use $\mathbb{P}_2 - \mathbb{P}_1$ elements for the fluid velocity and pressure, respectively, and $\mathbb{P}_2$ elements for the structure velocity and displacement on a mesh containing 1,000 elements in the fluid domain and 300 elements in the structure domain. The problem is solved using the proposed strongly-coupled scheme detailed in Algorithm 2, and a partitioned, explicit method [14,16,46] which was used in the development of the proposed algorithm. Since the explicit scheme exhibits $\mathcal{O}(\tau^{\frac{1}{2}})$ convergence rate, we apply it using both $\tau = 10^{-4}$ and $\tau = 10^{-6}$.

Figures 7, 8 and 9 show a comparison of the flowrate, pressure at the centerline, and the interface displacement magnitude at times $t = 4, 8$, and 12 ms. While we notice a discrepancy between the results obtained using Algorithm 2 and the explicit scheme with $\tau = 10^{-4}$, an excellent agreement is obtained between the two methods when $\tau = 10^{-6}$ is used in the explicit scheme. Since the proposed method can be considered as a second-order extension (when $\theta = \frac{1}{2}$) of the explicit scheme, this example demonstrates the improvement in accuracy achieved by using this approach.

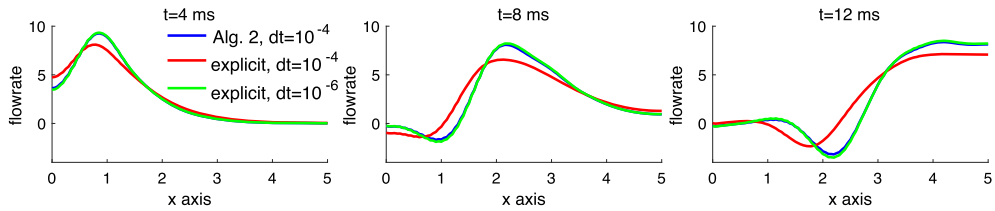


FIG. 7. Example 2. Fluid flowrate versus x-axis obtained with Algorithm 2 and the explicit scheme [14,16,46] used in the derivation of the proposed method

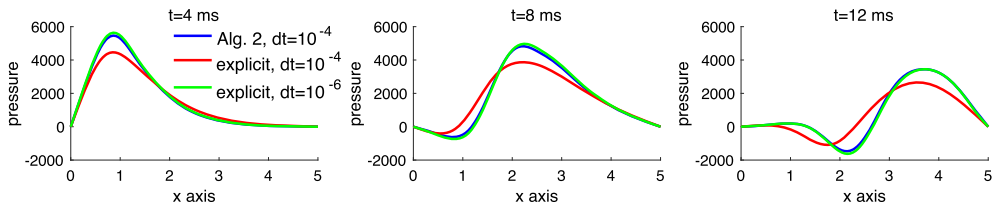


FIG. 8. Example 2. Fluid pressure at the centerline versus x-axis obtained with Algorithm 2 and the explicit scheme [14,16,46] used in the derivation of the proposed method

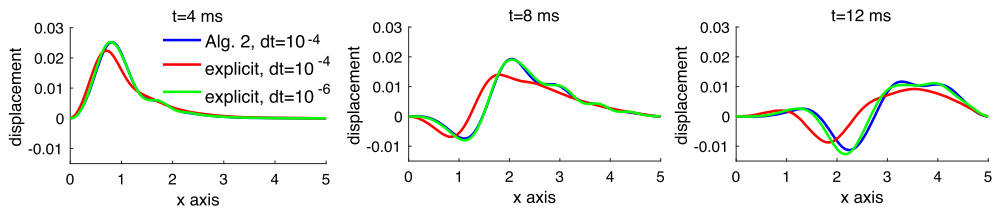


FIG. 9. Example 2. Fluid–structure interface displacement magnitude versus x-axis obtained with Algorithm 2 and the explicit scheme [14,16,46] used in the derivation of the proposed method

## 8. Conclusions

In this work, we propose a novel strongly-coupled method for FSI problems with thick structures. The method is based on the Robin coupling conditions, which are split so that both the fluid and structure sub-problems are implemented using a Robin-type boundary condition at the interface. In order to discretize the FSI problem in time, our scheme implements a refactorization of the Cauchy's one-legged '$\theta$-like' method, where the fluid and structure sub-problems are solved in the BE-FE fashion. The BE part of the algorithm is iterated until convergence, and the FE part is equivalent to linear extrapolations, making it computationally inexpensive to solve. In this approach, the proposed method is second-order accurate when $\theta = \frac{1}{2}$. Using energy estimates, we show that the sub-iterative part of the scheme is convergent and that the method is stable provided $\theta \in [\frac{1}{2}, 1]$. We also present an extension of the method to moving domain FSI problems.

The theoretical expectations have been validated in numerical examples. To discretize the problem in space, we use the finite element method. We began by computing the convergence rates using the method of manufactured solutions on a linear problem. In order to explore the variables in our scheme, we analyzed rates amongst different values of the combination parameter, $\alpha$, the time-discretization parameter, $\theta$, and tolerance, $\epsilon$, used to measure convergence of the BE steps. We considered a wide range of values for the combination parameter, $\alpha$, as well as an optimal value $\alpha_{opt}$ proposed in [31], which showed to be effective at maintaining optimal convergence rates and reasonably reducing the error compared to other

tested values. We obtained rates of $\mathcal{O}(\tau^2)$ when $\theta = \frac{1}{2}$, while the rates decreased to orders of convergence between $\mathcal{O}(\tau)$ and $\mathcal{O}(\tau^2)$ for other values of $\theta$. We also experienced sub-optimality in some cases if the tolerance was too large, in particular for $\epsilon = 10^{-3}$. However, our results show that decreasing $\epsilon$ at the same rate as $\tau$ corrects the sub-optimalities and yields the optimal convergence rate.

To better understand the relation between the parameters in the problem and the computational cost of our method, we computed the average number of sub-iterations in the BE part of the scheme. Our results show that the number of sub-iterations is reduced as the time step, $\tau$, decreases, and in most cases considered in our study, approaches 2. We also observe that while the case when $\epsilon = 10^{-4}$ requires more sub-iterations than when $\epsilon = 10^{-3}$, if we start from the latter value and decrease it at the same rate as $\tau$, the number of sub-iterations remains roughly the same, while preserving optimal convergence rates. We compared the number of sub-iterations required by our scheme to the ones needed by the Robin–Neumann method and the Robin–Robin method across different parameter values and observed that in every case, our scheme has fewer sub-iterations. Finally, we solved an FSI problem on a moving domain benchmark example of a flow in a channel using parameters within physiologically realistic values of blood flow in compliant arteries. In this example, the results obtained using the proposed method were compared to the ones obtained using an explicit scheme which was used in its derivation. Our results indicate a significant improvement in accuracy achieved with the proposed method.

A drawback of this work is that the analysis is performed assuming that the fluid–structure coupling is linear and that the fluid domain is fixed. The extensions of the method to variable time-stepping strategies are a focus of our on-going research.

**Acknowledgements.** This work was partially supported by NSF under Grants DMS 1912908 and DCSD 1934300.

### Declarations

**Conflict of interest** The authors declare that they have no conflict of interest.

**Publisher's Note** Springer Nature remains neutral with regard to jurisdictional claims in published maps and institutional affiliations.

## References

[1] Badia, S., Nobile, F., Vergara, C.: Fluid–structure partitioned procedures based on Robin transmission conditions. J. Comput. Phys. **227**, 7027–7051 (2008)
[2] Badia, S., Nobile, F., Vergara, C.: Robin–Robin preconditioned Krylov methods for fluid–structure interaction problems. Comput. Methods Appl. Mech. Eng. **198**(33), 2768–2784 (2009)
[3] Baek, H., Karniadakis, G.: A convergence study of a new partitioned fluid–structure interaction algorithm based on fictitious mass and damping. J. Comput. Phys. **231**(2), 629–652 (2012)
[4] Banks, J., Henshaw, W., Schwendeman, D.: An analysis of a new stable partitioned algorithm for FSI problems. Part I: incompressible flow and elastic solids. J. Comput. Phys. **269**, 108–137 (2014)
[5] Banks, J., Henshaw, W., Schwendeman, D.: An analysis of a new stable partitioned algorithm for FSI problems. Part II: incompressible flow and structural shells. J. Comput. Phys. **268**, 399–416 (2014)
[6] Bathe, K.-J., Zhang, H.: Finite element developments for general fluid flows with structural interactions. Int. J. Numer. Methods Eng. **60**(1), 213–232 (2004)
[7] Bazilevs, Y., Calo, V., Hughes, T., Zhang, Y.: Isogeometric fluid–structure interaction: theory, algorithms, and computations. Comput. Mech. **43**(1), 3–37 (2008)
[8] Bukač, M., Čanić, S., Glowinski, R., Muha, B., Quaini, A.: A modular, operator-splitting scheme for fluid–structure interaction problems with thick structures. Int. J. Numer. Methods Fluids **74**(8), 577–604 (2014)
[9] Bukač, M., Čanić, S., Muha, B.: A partitioned scheme for fluid–composite structure interaction problems. J. Comput. Phys. **281**, 493–517 (2015)
[10] Bukac, M., Muha, B.: Stability and convergence analysis of the extensions of the kinematically coupled scheme for the fluid–structure interaction. SIAM J. Numer. Anal. **54**(5), 3032–3061 (2016)
[11] Bukač, M., Yotov, I., Zunino, P.: An operator splitting approach for the interaction between a fluid and a multilayered poroelastic structure. Numer. Methods Partial Differ. Equ. **31**(4), 1054–1100 (2015)

[12] Burkardt, J., Trenchea, C.: Refactorization of the midpoint rule. Appl. Math. Lett. **107**, 106438 (2020)
[13] Burman, E., Durst, R., Fernández, M., Guzmán, J.: Fully discrete loosely coupled Robin-Robin scheme for incompressible fluid-structure interaction: stability and error analysis (2020). arXiv:2007.03846
[14] Burman, E., Durst, R., Guzman, J.: Stability and error analysis of a splitting method using Robin–Robin coupling applied to a fluid–structure interaction problem (2019). arXiv:1911.06760
[15] Burman, E., Fernández, M.: Stabilization of explicit coupling in fluid–structure interaction involving fluid incompressibility. Comput. Methods Appl. Mech. Eng. **198**, 766–784 (2009)
[16] Burman, E., Fernández, M.: Explicit strategies for incompressible fluid-structure interaction problems: Nitsche type mortaring versus Robin–Robin coupling. Int. J. Numer. Meth. Eng. **97**(10), 739–758 (2014)
[17] Burman, E., Fernández, M.: An unfitted Nitsche method for incompressible fluid–structure interaction using overlapping meshes. Comput. Methods Appl. Mech. Eng. **279**, 497–514 (2014)
[18] Cauchy, A.-L., Équations différentielles ordinaires. Éditions Études Vivantes, Ltée., Ville Saint-Laurent, QC; Johnson Reprint Corp., New York, Unpublished course. Fragment, With a preface by J. Dieudonné, With an introduction by C. Gilain (1981)
[19] Causin, P., Gerbeau, J.F., Nobile, F.: Added-mass effect in the design of partitioned algorithms for fluid–structure problems. Comput. Methods Appl. Mech. Eng. **194**(42–44), 4506–4527 (2005)
[20] Crank, J., Nicolson, P.: A practical method for numerical evaluation of solutions of partial differential equations of the heat-conduction type. In: Mathematical Proceedings of the Cambridge Philosophical Society, vol. 43, pp. 50–67. Cambridge University Press (1947)
[21] Dahlquist, G., Liniger, W., Nevanlinna, O.: Stability of two-step methods for variable integration steps. SIAM J. Numer. Anal. **20**(5), 1071–1085 (1983)
[22] Degroote, J.: On the similarity between Dirichlet–Neumann with interface artificial compressibility and Robin–Neumann schemes for the solution of fluid–structure interaction problems. J. Comput. Phys. **230**(17), 6399–6403 (2011)
[23] Degroote, J., Bruggeman, P., Haelterman, R., Vierendeels, J.: Stability of a coupling technique for partitioned solvers in FSI applications. Comput. Struct. **86**(23), 2224–2234 (2008)
[24] Deparis, S., Fernández, M., Formaggia, L.: Acceleration of a fixed point algorithm for fluid–structure interaction using transpiration conditions. ESAIM: Mathematical Modelling and Numerical Analysis-Modélisation Mathématique et Analyse Numérique **37**(4), 601–616 (2003)
[25] Farhat, C., Van der Zee, K., Geuzaine, P.: Provably second-order time-accurate loosely-coupled solution algorithms for transient nonlinear computational aeroelasticity. Comput. Methods Appl. Mech. Eng. **195**(17), 1973–2001 (2006)
[26] Fernández, M.: Incremental displacement-correction schemes for incompressible fluid–structure interaction: stability and convergence analysis. Numer. Math. **123**, 210–65 (2012)
[27] Fernández, M., Landajuela, M.: A fully decoupled scheme for the interaction of a thin-walled structure with an incompressible fluid. C.R. Math. **351**(3–4), 161–164 (2013)
[28] Fernández, M., Mullaert, J., Vidrascu, M.: Generalized Robin–Neumann explicit coupling schemes for incompressible fluid-structure interaction: stability analysis and numerics. Int. J. Numer. Methods Eng. **101**(3), 199–229 (2015)
[29] Formaggia, L., Quarteroni, A., Veneziani, A.: Cardiovascular Mathematics: Modeling and Simulation of the Circulatory System, vol. 1. Springer, Berlin (2010)
[30] Gee, M., Küttler, U., Wall, W.: Truly monolithic algebraic multigrid for fluid–structure interaction. Int. J. Numer. Methods Eng. **85**(8), 987–1016 (2011)
[31] Gerardo-Giorda, L., Nobile, F., Vergara, C.: Analysis and optimization of Robin–Robin partitioned procedures in fluid–structure interaction problems. SIAM J. Numer. Anal. **48**(6), 2091–2116 (2010)
[32] Gerbeau, J.-F., Vidrascu, M.: A Quasi–Newton algorithm based on a reduced model for fluid–structure interaction problems in blood flows. ESAIM: Mathematical Modelling and Numerical Analysis-Modélisation Mathématique et Analyse Numérique **37**(4), 631–647 (2003)
[33] Gigante, G., Vergara, C.: On the stability of a loosely-coupled scheme based on a Robin interface condition for fluid–structure interaction (2019). arXiv:1905.06593
[34] Girault, V., Raviart, P.-A.: Finite Element Approximation of the Navier–Stokes Equations. Lecture Notes in Mathematics, p. 749. Springer, Berlin (1979)
[35] Hansbo, P.: Nitsche's method for interface problems in computational mechanics. GAMM-Mitt. **28**(2), 183–206 (2005)
[36] Hecht, F.: New development in FreeFem++. J. Numer. Math. **20**(3–4), 251–266 (2012)
[37] Hron, J., Turek, S.: A Monolithic FEM/Multigrid Solver for an ALE Formulation of Fluid-Structure Interaction with Applications in Biomechanics. In: Fluid–Structure Interaction. volume 53 of Lecture Notes in Computational Science and Engineering, pp. 146–170. Springer, Berlin (2006)
[38] Hundsdorfer, W., Verwer, J.: Numerical Solution of Time-Dependent Advection–Diffusion–Reaction Equations, vol. 33. Springer, Berlin (2013)
[39] Langer, U., Yang, H.: Numerical simulation of fluid–structure interaction problems with hyperelastic models: a monolithic approach. Math. Comput. Simul. **145**, 186–208 (2018)
[40] Lukáčová-Medvid'ová, M., Rusnáková, G., Hundertmark-Zaušková, A.: Kinematic splitting algorithm for fluid–structure interaction in hemodynamics. Comput. Methods Appl. Mech. Eng. **265**, 83–106 (2013)
[41] Muha, B., Čanić, S.: Existence of a solution to a fluid-multi-layered-structure interaction problem. J. Differ. Equ. **256**(2), 658–706 (2014)
[42] Nobile, F.: Numerical approximation of fluid–structure interaction problems with application to haemodynamics. Ph.D. thesis, EPFL, Switzerland (2001)

[43] Nobile, F., Vergara, C.: An effective fluid–structure interaction formulation for vascular dynamics by generalized Robin conditions. SIAM J. Sci. Comput. **30**, 731–763 (2008)
[44] Oyekole, O., Trenchea, C., Bukač, M.: A second-order in time approximation of fluid–structure interaction problem. SIAM J. Numer. Anal. **56**(1), 590–613 (2018)
[45] Ryzhakov, P., Rossi, R., Idelsohn, S., Oñate, E.: A monolithic Lagrangian approach for fluid–structure interaction problems. Comput. Mech. **46**(6), 883–899 (2010)
[46] Seboldt, A., Bukač, M.: A non-iterative domain decomposition method for the interaction between a fluid and a thick structure (2020). arXiv:2007.00781
[47] Serino, D., Banks, J., Henshaw, W., Schwendeman, D.: A stable added-mass partitioned (AMP) algorithm for elastic solids and incompressible flow: model problem analysis. SIAM J. Sci. Comput. **41**(4), A2464–A2484 (2019)
[48] Stetter, H.: Analysis of Discretization Methods for Ordinary Differential Equations, vol. 23. Springer, Berlin (1973)
[49] Yu, Y., Baek, H., Karniadakis, G.: Generalized fictitious methods for fluid–structure interactions: analysis and simulations. J. Comput. Phys. **245**, 317–346 (2013)

Martina Bukač and Anyastassia Seboldt
Department of Applied and Computational Mathematics and Statistics
University of Notre Dame
Notre Dame IN46556
USA

e-mail: mbukac@nd.edu

Anyastassia Seboldt
e-mail: aseboldt@nd.edu

Catalin Trenchea
Department of Mathematics
University of Pittsburgh
Pittsburgh PA15260
USA
e-mail: trenchea@pitt.edu

(accepted: May 7, 2021)